MJO teleconnections over the PNA region in climate models. Part II: Impacts of the MJO and basic state

Jiabao Wang[1], Hyemi Kim[1*], Daehyun Kim[2], Stephanie A. Henderson[3], Cristiana Stan[4], and Eric D. Maloney[5]

[1]*School of Marine and Atmospheric Sciences, Stony Brook University, Stony Brook, Stony Brook, New York*

[2]*Department of Atmospheric Sciences, University of Washington, Seattle, Washington*

[3]*Department of Atmospheric and Oceanic Sciences, University of Wisconsin–Madison, Madison, Wisconsin*

[4] *Department of Atmospheric, Oceanic, and Earth Sciences, George Mason University, Fairfax, Virginia*

[5]*Department of Atmospheric Science, Colorado State University, Fort Collins, Colorado*

Submitted to Process-Oriented Model Diagnostics special collection

Journal of Climate

* Corresponding author:

Hyemi Kim (hyemi.kim@stonybrook.edu)

119 Endeavor Hall, School of Marine and Atmospheric Sciences, Stony Brook University, Stony Brook, NY, 11794-5000, USA

Early Online Release: This preliminary version has been accepted for publication in *Journal of Climate*, may be fully cited, and has been assigned DOI 10.1175/JCLI-D-19-0865.1. The final typeset copyedited article will replace the EOR at the above DOI when it is published.

ABSTRACT

In an assessment of 29 global climate models (GCMs), Part I of this study identified biases in boreal winter MJO teleconnections in anomalous 500-hPa geopotential height over the Pacific-North America (PNA) region that are common to many models: an eastward shift, a longer persistence, and a larger amplitude. In Part II, we explore the relationships of the teleconnection metrics developed in Part I with several existing and newly-developed MJO and basic state (the mean subtropical westerly jet) metrics. The MJO and basic state diagnostics indicate that the MJO is generally weaker, less coherent, and propagates faster in models compared to observations. The mean subtropical jet also exhibits notable biases such as too strong amplitude, excessive eastward extension, or southward shift. The following relationships are found to be robust among the models: 1) models with a faster MJO propagation tend to produce weaker teleconnections; 2) models with a less coherent eastward MJO propagation tend to simulate more persistent MJO teleconnections; 3) models with a stronger westerly jet produce stronger and eastward shifted MJO teleconnections; 4) models with an eastward extended jet produce an eastward shift in MJO teleconnections; and 5) models with a southward shifted jet produce stronger MJO teleconnections. The results are supported by linear baroclinic model experiments. Our results suggest that the larger amplitude and eastward shift biases in GCM MJO teleconnections can be attributed to the biases in the westerly jet, and that the longer persistence bias is likely due to the lack of coherent eastward MJO propagation.

Accepted for publication in *Journal of Climate*. DOI 10.1175/JCLI-D-19-0865.1.

1. Introduction

The Madden-Julian Oscillation (MJO; Madden and Julian 1971, 1972) is characterized by the eastward propagation of a planetary-scale convectively coupled system in the equatorial Indo-Pacific warm pool with an average phase speed of about 5 m/s. It takes approximately 30 to 60 days for an MJO event to travel from the western Indian Ocean to the dateline, around where the convective signal tends to cease. Diabatic heating related to the MJO leads to the formation of an anomalous Rossby wave source (RWS) in the subtropics and mid-latitudes through anomalous upper-level divergent winds in regions with a strong absolute vorticity gradient near the subtropical westerly jet (e.g., Sardeshmukh and Hoskins 1988). Excited Rossby waves propagate poleward and eastward into the extratropics and modulate circulations there (e.g., Horel and Wallace 1981; Hoskins and Karoly 1981). MJO teleconnections can significantly modulate mid-latitude weather and climate phenomena such as blocking events (Henderson et al. 2016), precipitation and temperature (Zhou et al. 2012; Zheng et al. 2018), atmospheric rivers (Mundhenk et al. 2016), storm tracks (Deng and Jiang 2011; Wang et al. 2018a; Zheng et al. 2018), the North Atlantic Oscillation (Cassou 2008; Lin et al. 2009), and the Pacific-North American (PNA) pattern (Mori and Watanabe 2008; Tseng et al. 2019; Henderson et al. 2019, submitted). Given the broad impacts of MJO teleconnections, a better understanding of the factors that influence MJO teleconnections and their accurate simulation in global climate models (GCMs) is crucial to both the research and operational communities. The Working Group on Numerical Experimentation (WGNE) MJO Task Force adopted this as one of the priority subprojects as a joint activity with the World Meteorological Organization (WMO) Subseasonal-to-Seasonal (S2S) teleconnection

Accepted for publication in *Journal of Climate*. DOI 10.1175/JCLI-D-19-0865.1.

subproject. The scientific focuses of the joint activity include: 1) development of standardized MJO teleconnection diagnostics (Wang et al. 2019, Part I of this work) and 2) analysis of the sensitivity of MJO teleconnections to MJO and basic state representations in models and sources of teleconnection biases (the focus of Part II).

It is reasonable to expect MJO teleconnections over the PNA region in a model to be affected by the model's own MJO characteristics such as its amplitude, propagation speed, and extent. The amplitude of MJO teleconnections would be stronger when the MJO and associated RWS is stronger (Wang et al. 2018a). MJO teleconnections would also intensify if the MJO propagates farther eastward into the central Pacific rather than weakens or breaks down over the Maritime Continent ("Maritime Continent barrier effect", Rui and Wang 1990; Kim et al. 2014a). This is because extraction of kinetic energy from the mean flow by the Rossby wave is known to be particularly efficient in the jet exit region (Adames and Wallace 2014; Bao and Hartmann 2014). On the other hand, MJO teleconnections would be weaker if the MJO propagates with a phase speed that is faster than the average (Bladé and Hartmann 1995; Yadav and Straus 2017; Goss and Feldstein 2018; Zheng and Chang 2019). According to Bladé and Hartmann (1995), this is because 1) a faster propagating MJO is equivalent to embedding the forcing in strong relative easterly winds, which gives rise to an enhanced equatorial trapping of Rossby waves, and 2) the faster propagating MJO leads to a decrease in the Rossby wave group velocity which causes a greater wave damping during its propagation. The weaker teleconnection amplitude may also arise from the weaker teleconnection persistence as the MJO heating and associated RWS would transit more rapidly from one phase to the next phase for a fast propagating MJO (Zheng and Chang 2019).

Accepted for publication in *Journal of Climate*. DOI 10.1175/JCLI-D-19-0865.1.

93 MJO teleconnections are also influenced by the basic state in the extratropics. In boreal
94 winter, anomalous vorticity generation reaches a maximum at the southern boundary of the
95 subtropical westerly jet where the absolute vorticity gradient is at maximum (Sardeshmukh
96 and Hoskins 1988). The excited Rossby waves are refracted toward regions of high
97 stationary wavenumber K_S. Thus the westerly jet, where K_S is maximized, acts as a
98 waveguide (Hoskins and Ambrizzi 1993). On the poleward and equatorward sides of the
99 jet, the meridional gradient of absolute vorticity ($\beta^* = \frac{\partial f}{\partial y} - \frac{\partial^2 \bar{u}}{\partial y^2}$) is small or can become
100 negative due to strong meridional curvature ($\frac{\partial^2 \bar{u}}{\partial y^2}$). This is the region where Rossby waves
101 are reflected, and they must propagate eastward along the jet and emanate at the exit region
102 (Karoly 1983; Simmons et al. 1983; Hoskins and Ambrizzi 1993; Seo and Lee 2017).
103 Above considerations strongly suggest that simulation of MJO teleconnections in GCMs
104 can be improved with a more realistic MJO (Yoo et al. 2015; Stan and Straus 2019) or the
105 basic state in the extratropics, in particular the amplitude and position of the westerly jet.
106 While it has been documented that many current GCMs still produce a weaker MJO with
107 faster and less coherent eastward propagation (e.g., Kim et al. 2014b; Ahn et al. 2017) than
108 the observed and a stronger Pacific westerly jet with an eastward extension (Gong et al.
109 2014; Henderson et al. 2017), a systematic examination of the relationship between MJO
110 teleconnections and the characteristics of the MJO and the subtropical jet using a large set
111 of GCM simulations has not been performed.
112 In Part I, a set of standardized MJO teleconnection metrics was developed for objectively
113 evaluating and comparing boreal winter MJO teleconnections (defined using the 500-hPa
114 geopotential height anomalies; Z500a) over the PNA region (120°E-60°W, 20°-80°N) in
115 the 29 GCMs relative to reanalysis fields. It is shown that current GCMs generally produce

Accepted for publication in *Journal of Climate*. DOI 10.1175/JCLI-D-19-0865.1.

MJO teleconnections with an eastward shift, larger amplitude, and longer persistence compared to those observed. In Part II, we investigate how these MJO teleconnection biases relate to MJO and basic state characteristics. The hypotheses arising from this initial investigation are further tested with a linear baroclinic model (LBM; Watanabe and Kimoto 2000).

The paper is organized as follows. The GCMs and reference data are introduced in section 2. Five MJO skill metrics and their relationships with MJO teleconnections are discussed in section 3. Four basic state metrics and their relationships with MJO teleconnections are discussed in section 4. A description of the LBM and the results of sensitivity experiments are provided in section 5, followed by a summary and discussion in section 6.

2. GCMs and reference dataset

Since we use the same models and reference dataset as in Part I, they are only briefly described here. A total of 29 GCMs are analyzed (Table 1): 22 CMIP5 models (Taylor et al. 2012), 6 models from the Global Energy and Water Cycle Experiment Atmospheric System Study and Year of Tropical Convection (GASS/YoTC) project (Jiang et al. 2015), and one Atmospheric Model Intercomparison Project (AMIP) run from the European Centre for Medium-Range Weather Forecasts (ECMWF) (Davini et al. 2017). The period analyzed in this study is 1975-2005 for CMIP5 models, 1991-2010 for GASS/YoTC models (except for SPCAM, for which 1986-2003 is used), and 1980-2000 for the ECMWF model. Only one ensemble member from each model is analyzed.

Accepted for publication in *Journal of Climate*. DOI 10.1175/JCLI-D-19-0865.1.

The NOAA Advanced Very High Resolution Radiometer OLR (Liebmann and Smith 1996) dataset and ECMWF Interim reanalysis data (Dee et al. 2011) from 1979 to 2017 are analyzed (hereafter referred to as "observations"). We focus on October to March when the MJO and Northern Hemisphere teleconnections are most prominent. Model output and reference data are interpolated to the same horizontal resolution (2.5°×2.5°). Anomalies are derived by subtracting the first three harmonics of the climatological seasonal cycle and the most recent 120-day mean from each field to reduce the influence of interannual variability (Wheeler and Hendon 2004). No filtering is applied unless stated otherwise.

3. MJO simulation and its influence on MJO teleconnections

a. MJO simulation (MJO skill metrics M1-M5)

Several MJO metrics developed by previous studies (e.g., Kim et al. 2009; Waliser et al. 2009; Jiang et al. 2015; Ahn et al. 2017) are applied to the 29 GCMs. Fig. 1 shows Hovmöller diagrams (longitude vs. time lag) of 10°S-10°N averaged 25-90 day filtered OLR anomalies using a Lanczos filter (Duchon 1979). Day 0 corresponds to the day when the standard deviation of OLR anomaly averaged over the eastern Indian Ocean (75°-85°E, 5S°-5°N) is less than -1, day 1 is the lag composite of OLR anomaly one day after day 0, and so on. A majority of models do not simulate realistic eastward MJO propagation. Some models (e.g., GFDL-ESM2G, GFDL-ESM2M, HadGEM2-AO, MIROC-ESM, MIROC-ESM-CHEM, and NCAR-CAM5) produce a stationary MJO. CanESM2 shows westward propagation. To quantify how well a model simulates eastward MJO propagation, a metric M1 is developed following Jiang et al. (2015):

Accepted for publication in *Journal of Climate*. DOI 10.1175/JCLI-D-19-0865.1.

(M1) MJO propagation skill: The pattern correlation coefficient (pattern CC) is calculated between the observed and model's Hovmöller diagram of OLR anomalies: one for the composites against convection averaged over the eastern Indian Ocean (Fig. 1) and another against the corresponding western Pacific (130°-150°E, 5S°-5°N) time series (not shown) (more details in Jiang et al. 2015). Metric M1 is derived as the average of these two pattern CCs and ranges from 0.5 to 0.9 among models (Fig. 2a). "Good" MJO models are defined when M1 exceeds 0.75 (a total of 12 models, bolded in Table 1). These models are consistent with the "good" MJO models analyzed in Jiang et al. (2015) and Henderson et al. (2017) who used lag regression and lag correlation, respectively, to construct the Hovmöller diagrams for selecting the "good" MJO models.

(M2) Coherency: this metric aims to characterize the coherency of the eastward MJO propagation. Following Sperber and Kim (2012) and Ahn et al. (2017), M2 is the average of the absolute values of maximum and minimum lead-lag correlation coefficients calculated between the Real-time Multivariate MJO (RMM, Wheeler and Hendon 2004) indices. Same as part I, the model RMM indices are constructed by projecting the 15°S-15°N averaged OLR and 850-hPa and 200-hPa zonal wind anomalies onto the observed combined EOF (CEOF) eigenvectors (hereafter referred to as "projected RMM indices"). This projection technique (Duffy et al. 2003) allows a direct and consistent comparison of the MJO among models and observations. M2 calculated using the projected RMM indices (Fig. 2b) is highly correlated (correlation coefficient at 0.91) with that using RMM indices derived from each model's eigenvectors. A smaller M2 value indicates a weaker relationship between the two RMM indices, and thus less coherent eastward propagation of MJO convection from the Indian Ocean to the western Pacific. Most models (~89%)

Accepted for publication in *Journal of Climate*. DOI 10.1175/JCLI-D-19-0865.1.

have M2 values that are lower than that from observations (0.54), which is consistent with the findings of Ahn et al. (2017).

Metric M3 is calculated based on the wavenumber-frequency power spectrum of 10°S-10°N averaged OLR following Ahn et al. (2017). Power spectra for observations, the six GASS/YoTC models, and the ECMWF model are compared in Fig. 3. Corresponding CMIP5 model results can be found in Fig. 1 of Ahn et al. (2017) for precipitation and 850-hPa zonal wind. In observations (Fig. 3a), the power peaks within the 30-80-day period at wavenumbers 1-3 (usually referred to as the "MJO band"), which is consistent with previous studies (e.g., Zhang et al. 2006; Kim et al. 2009; Ahn et al. 2017). The models have large biases in the spatial and temporal scale of the MJO. Eastward power in GISS-E2, MRI-AGCM3, SPCCSM3, and ECMWF peaks at a much lower frequency/longer period (~100-day period) at zonal wavenumbers 1-3. ECMWF, TAMU, and SPCAM3 strongly overestimate the eastward power within the MJO band, while GISS-E2 and NCAR-CAM5 underestimate it. A metric M3 is developed to quantify the MJO period in model simulations:

(M3) MJO Period: The average period is calculated as the sum of the power-weighted period divided by the sum of power over the 25-100-day period for zonal wavenumbers 1-3 (red box in Fig. 3a). This broad period range is selected given the large model spread in the dominant MJO period. The observed MJO period is approximately 43 days. About 75% of models have a shorter MJO period than observations (Fig. 2c), indicating faster MJO propagation than the observed average phase speed in most GCMs consistent with Ahn et al. (2017). Simulated MJO period is especially short in MIROC-ESM and MIROC-ESM-CHEM at around 36 days, and longer in TAMU-CAM4 at around 48 days. The MJO period

Accepted for publication in *Journal of Climate*. DOI 10.1175/JCLI-D-19-0865.1.

206 estimated from the lead-lag correlation between the projected RMM indices (Ahn et al.
207 2017) are highly correlated with M3 across all models (correlation coefficient at 0.74).
208 Metrics M4 and M5 are developed from the composites of OLR anomalies of strong
209 MJO events defined when the amplitude of the projected RMM indices exceeds 1.0.
210 (M4) OLR pattern CC: Pattern CC is calculated between the modeled and observed OLR
211 anomalies (Fig. 1 of Part I) over the tropical Indo-Pacific region (40°E-140°W, 15°S-15°N).
212 Results for MJO phases 3 and 7 are summarized in Fig. 4. These phases are the most
213 effective MJO phases in exciting extratropical circulation anomalies (Stan et al. 2017;
214 Tseng et al. 2019). All models reasonably simulate the MJO OLR pattern (M4 > 0.5). In
215 particular, ACCESS1-3, CMCC-CESM, MIROC5, MRI-ESM1, NorESM1-M, TAMU-
216 CAM4, and ECMWF simulate a rather realistic MJO pattern for both phases 3 and 7 (M4 >
217 0.8). Among the eight MJO phases, models simulate a more realistic MJO OLR pattern for
218 phases 2, 3, and 6 (multi-model mean of M4 greater than 0.75).
219 (M5) OLR amplitude: OLR amplitude is calculated as the standard deviation of composite
220 OLR anomalies over the Indo-Pacific region in a model divided by that of observations
221 (Taylor 2001). A value less than 1 indicates an underestimate of the OLR amplitude in a
222 model. Most models (~70%) underestimate the amplitude of MJO convection for both
223 phases 3 and 7 (Fig. 4) compared to observations. This overall weaker MJO is found in all
224 MJO phases (not shown). TAMU-CAM4 has an exceptionally strong MJO amplitude
225 because the model heating is constrained by the observed MJO heating structure. This
226 improves some aspects of MJO characteristics, such as a more realistic eastward
227 propagation (Lappen and Schumacher 2012), but produces too strong amplitude (Jiang et
228 al. 2015).

Accepted for publication in *Journal of Climate*. DOI 10.1175/JCLI-D-19-0865.1.

b. Relationships between the MJO and MJO teleconnections

Most of the models produce a weaker MJO with faster and less coherent eastward propagation, consistent with previous studies (e.g., Ahn et al. 2017). Impacts of these MJO biases on MJO teleconnections are now examined. MJO teleconnection metrics (T1-T6) are defined by 5–9-day averaged lagged response of Z500a over the PNA region to each MJO phase (more details in Part I). Pattern CC of MJO teleconnections (T1) and of RWS (T6) represents the general simulation skill of the teleconnection pattern. Relative amplitude (T2) is defined similar to OLR amplitude (M5) such that T2 >1.0 indicates stronger MJO teleconnections in a model than observations. East-west position (T3) is defined as the Z500a-weighted average longitude, which indicates the east-west shift of MJO teleconnections relative to observations; more positive value of T3 represents a more eastward shift. Intra-phase pattern consistency (IPC) (T4) measures the consistency of teleconnection patterns between individual MJO events for a given MJO phase; larger IPC indicates a higher consistency. Persistence (T5) represents the duration that teleconnections persist. Table 2 shows the linear correlation coefficients calculated between the MJO and teleconnection metrics across all models. Only metrics with statistically significant correlation coefficients are listed. For correlations with teleconnection amplitude (T2), the outlier model HadGEM2-AO is removed from the calculation due to an exceptionally large bias in the teleconnection amplitude (Part I).

Table 2 suggests that the model MJO affects the pattern of MJO teleconnections via affecting the RWS pattern. Models with a better and more coherent eastward MJO propagation (M1 and M2 are correlated at 0.77) and realistic MJO pattern (M4) generally simulate more realistic patterns of teleconnections (T1) and the RWS (T6). Models with a

Accepted for publication in *Journal of Climate*. DOI 10.1175/JCLI-D-19-0865.1.

slower MJO propagation (M3) tend to produce stronger MJO teleconnections (T2) (this will be tested in section 5; Bladé and Hartmann 1995; Yadav and Straus 2017; Goss and Feldstein 2018; Zheng and Chang 2019). Models with stronger MJO amplitude (M5) produce stronger MJO teleconnections (T2) with more consistent teleconnection patterns between individual MJO events (T4) and longer persistence (T5). This influence is possibly because stronger MJO convection can intensify the extratropical response (Wang et al. 2018a), which may lead to a slower decay and longer persistence of teleconnections. This, in turn, gives rise to a higher consistency of teleconnection patterns between individual MJO events.

Models with a better and more coherent MJO propagation (M1 and M2) have more realistic teleconnection persistence (T5) for phases 3 and 7. The averaged persistence of phases 3 and 7 for "good" MJO propagation models is 15 days, which is closer to the observed (13 days) compared to the rest of models (~ 20 days). The more realistic teleconnection persistence is possibly because MJO teleconnection changes correspond to a clear MJO transition from one phase to another. This hypothesis is tested with an LBM experiment in section 5. As a side note, although both MJO propagation (M1 and M2) and MJO amplitude (M5) are associated with teleconnection persistence (T5), no significant correlation is found between the MJO propagation and amplitude.

4. Basic state simulation and its influence on MJO teleconnections

a. Basic state simulation (basic state skill metrics B1-B4)

Generation and propagation of Rossby waves are strongly dependent on the position and intensity of the subtropical westerly jet. Simulation of upper-level zonal wind and its

Accepted for publication in *Journal of Climate*. DOI 10.1175/JCLI-D-19-0865.1.

influence on MJO teleconnections is investigated in this section. Fig. 5 shows the climatology of 250-hPa zonal wind (U250) in observations and biases in models. Significant biases in both the amplitude and position of the subtropical jet are found. For example, IPSL-CM5A-LR, MRI-CGCM3, and MRI-ESM1 simulate a stronger jet with significant eastward extension, while MIROC-ESM and MIROC-ESM-CHEM produce a westward retracted jet. Four basic state metrics (B1-B4) are developed based on Fig. 5:

(B1) RMSE: Root-mean-square error (RMSE) quantifies the basic state bias due to biases in the amplitude and position of the jet. Following Henderson et al. (2017), we first identify the latitude of the maximum U250 for each model and observations, extend the latitudes 10° to both the north and south of this maximum latitude, then calculate the RMSE between the model and observations over these latitudes across the longitude span of 100°E-120°W. RMSE is extremely large for IPSL-CM5A-LR, MRI-CGCM3, and MRI-ESM1, and small for SPCCSM3 and NCAR-CAM5 (Fig. 6a). The amplitude and position bias are further separated into metrics B2-B4.

(B2) Jet amplitude: To estimate the biases induced from the jet amplitude, B2 is calculated as the average of climatological U250 over the region isolated in metric B1. The averaged amplitude of the jet is 35.9 m/s in observations. About 62% of models overestimate the amplitude of the westerly jet (Fig. 6b), consistent with Gong et al. (2014). The jet is especially strong in IPSL-CM5A-LR, MRI-CGCM3, and MRI-ESM1, and weak in TAMU-CAM4.

(B3) Zonal extension of the jet: According to Winters et al. (2019), the dominant changes in the North Pacific westerly jet with longitude are characterized by an eastward extension or westward retraction; while changes with latitude are characterized by a northward or

Accepted for publication in *Journal of Climate*. DOI 10.1175/JCLI-D-19-0865.1.

298 southward shift. To measure the longitudinal bias of the simulated jet position, B3 is
299 calculated as the U250-weighted average longitude

300 $$\frac{\sum_{\varphi_1}^{\varphi_2}\sum_{\theta_1}^{\theta_2}\theta\cdot U(\theta,\varphi)\cdot\cos(\varphi)}{\sum_{\varphi_1}^{\varphi_2}\sum_{\theta_1}^{\theta_2}U(\theta,\varphi)\cdot\cos(\varphi)},$$

301 where θ is the longitude, φ is the latitude, and U is the climatological U250. B3 is thus
302 defined as the sum of longitude multiplied by climatological U250 divided by the sum of
303 U250 across the longitudinal span of 100°E-120°W (100°-240° in calculation) within the
304 region selected in B1 and B2. About 72% of models have B3 larger than observation
305 (161.59°E) (Fig. 6c), suggesting an eastward jet extension. The eastward jet extension is
306 especially significant in CMCC-CESM, MRI-CGCM3, and MRI-ESM1 (Figs. 5 and 6c).
307 (B4) Meridional shift of the jet: Similar to B3, this metric aims to evaluate the basic state
308 biases induced by meridional shifts of the jet. We calculate the U250-weighted average
309 latitude as

310 $$\frac{\sum_{\varphi_1}^{\varphi_2}\sum_{\theta_1}^{\theta_2}\varphi\cdot U(\theta,\varphi)\cdot\cos(\varphi)}{\sum_{\varphi_1}^{\varphi_2}\sum_{\theta_1}^{\theta_2}U(\theta,\varphi)\cdot\cos(\varphi)},$$

311 which is the sum of latitude multiplied by climatological U250 divided by the sum of U250
312 over 100°E-120°W, 10°-60°N (black box in Fig. 5a). This region with a broader latitudinal
313 boundary than that used in B1-B3 is selected to better capture the meridional shifts of the
314 jet. B4 values less than observation (34.5°N) indicate a southward shift of the jet, and vice
315 versa. About 66% of models produce the jet with a southward shift (Fig. 6d), such as IPSL-
316 CM5A-LR and MIROC5. When calculating over 29 models, a strong relationship is found
317 between B2 and B3 (0.71), and B2 and B4 (-0.7), indicating that a strong jet is usually
318 associated with an eastward extension and/or southward shift.
319 *b. Relationships between the basic state and MJO teleconnections*

Accepted for publication in *Journal of Climate*. DOI 10.1175/JCLI-D-19-0865.1.

We explore the relationship between the basic state metrics introduced above with the MJO teleconnection metrics (Table 3). Variations in the jet affect mostly the east-west position (T3) of MJO teleconnections. A stronger westerly jet (B2), an eastward extended jet (B3), and a southward shifted jet (B4) all coincide with an eastward shift in MJO teleconnections (T3). A positive relationship (correlation coefficient at 0.36) is found between the jet amplitude (B2) and teleconnection amplitude (T2), indicating that models that produce a stronger westerly jet may also produce stronger MJO teleconnections. The above relationships will be further examined with the LBM experiments in section 5 along with the mechanisms.

RMSE of U250 over the subtropical jet region (B1) has negligible correlation (-0.05) with teleconnection pattern (T1) when all 29 models are considered. However, when the bias of the jet becomes large (RMSE > 4, 8 models), the basic state significantly correlates negatively with MJO teleconnection patterns (correlation coefficient at -0.83) such that a larger bias leads to a larger degradation of teleconnection pattern simulation.

5. MJO and basic state impacts on MJO teleconnections: LBM experiments

a. LBM description, setup, and control run

The LBM is constructed by linearizing the primitive equations about a basic state and the linear response to a prescribed MJO heating is derived to simulate MJO teleconnections (Mori and Watanabe 2008; Henderson et al. 2017). The model has a horizontal resolution of T42 (~2.8° grid resolution) and 20 unevenly spaced sigma (σ) levels in the vertical. The magnitude of the biharmonic diffusion coefficient defined by the *e*-folding decay time is set to 2 hours for the largest wavenumber. The dissipation timescale for Newtonian

Accepted for publication in *Journal of Climate*. DOI 10.1175/JCLI-D-19-0865.1.

damping and Rayleigh friction is set to 0.5 days for the lower boundary layers ($\sigma \geq 0.9$) and the top two levels ($\sigma \leq 0.3$), with the remaining layers having a timescale of 20 days (Mori and Watanabe 2008; Henderson et al. 2017). These parameters are not altered for sensitivity experiments.

In the LBM, the heating and basic state can be separately modified, which allows an investigation of the relative impact of MJO and basic state on MJO teleconnections. The model basic state for the control run uses the monthly climatology during October to March generated from observations over the period of 1979-2017. The model is forced by the observational daily apparent heat source Q_1 (Yanai et al. 1973) computed as

$$Q_1 = \frac{\partial s}{\partial t} + \boldsymbol{v} \cdot \nabla s + \omega \frac{\partial s}{\partial p},$$

where $\boldsymbol{v}$ is the horizontal velocity, ω is the vertical velocity, and s is the dry static energy defined as $s = C_p T + gz$, where C_p is the specific heat capacity of air at constant pressure, T is the temperature, g is the gravitational acceleration, and z is the height. An eastward propagating anomalous Q_1 is obtained following Henderson et al. (2017). We first removed the daily climatological seasonal cycle and constructed composites of anomalous Q_1 from MJO phase 1 to 8 based on the phase definition in Wheeler and Hendon (2004). Then the eight Q_1 phase composites are interpolated linearly with an assumption of 5 days per phase to mimic an observed boreal winter MJO cycle of about 40 days (Alaka and Maloney 2012; Henderson et al. 2016). This eastward propagating forcing (Fig. 7) is applied once in the LBM experiments, i.e., the forcing is not cyclic (a cyclic MJO forcing leads to same conclusions, not shown). We only specify Q_1 anomalies in 30°S-30°N to focus on the forcing from the tropics.

Accepted for publication in *Journal of Climate*. DOI 10.1175/JCLI-D-19-0865.1.

365 The LBM Z500a response averaged 5-9 days after MJO phase 3 (hereafter referred to as
366 "phase 3 teleconnection"; average over model days 16-24 considering 5-day/phase) and
367 the observational reference are shown in Fig. 8. Although the amplitude is weaker, the
368 control run reasonably captures the observed Z500a pattern over the PNA region (pattern
369 correlation is 0.79). In the following sections, various MJO and basic state sensitivity runs
370 (Table 4) are performed with this LBM to investigate the relative impact of MJO and basic
371 state changes on MJO teleconnections.

372 *b. Impact of MJO propagation on teleconnection persistence*

373 In section 3, we found that when a model produces a less coherent and poor eastward
374 MJO propagation, the teleconnections tend to persist longer. This finding is further
375 supported with an LBM experiment. To mimic a non-propagating MJO event (Kim et al.
376 2014a), the propagating anomalous Q_1 used in the control run is set to remain stationary
377 after reaching MJO phase 4 (referred to as "*Nonprop_MJO* run"), and thus the imposed
378 MJO heating does not propagate across the Maritime Continent. We use the observed MJO
379 heating rather than heating profiles from poor MJO propagation models to reduce the
380 possible influence from other biases of MJO characteristics such as horizontal and vertical
381 structure. Using the heating profiles obtained from a poor MJO propagation model (e.g.,
382 HadGEM2-AO) led to a similar conclusion. Note that by gradually decreasing the
383 amplitude of Q_1 with an e-folding time of 10 days after reaching MJO phase 4 does not
384 change the conclusion (not shown). The pattern CC between the phase 3 teleconnection
385 (e.g., Fig. 8a) and five-day running average of Z500a response starting from model day 16
386 is calculated over the PNA region (similar to the concept of autocorrelation). The results
387 for the control and *Nonprop_MJO* runs are shown in Fig. 9. Day 1 is the pattern CC

Accepted for publication in *Journal of Climate*. DOI 10.1175/JCLI-D-19-0865.1.

388 calculated between phase 3 teleconnection and 16-20-day averaged Z500a response, day 2
389 is pattern CC between phase 3 teleconnection and 17-21-day averaged Z500a response,
390 and so on. The persistence of MJO teleconnections is defined as the length of the time
391 period (unit: days) during which the pattern CC remains larger than 0.5 (details in Part I).
392 In the control run, phase 3 teleconnection persists for 10 days before transitioning to a
393 different pattern or decay as the MJO propagates consistently with observations. In the
394 *Nonprop_MJO* run, phase 3 teleconnection persists two times longer (until 20 days) than
395 the control run. This sensitivity of teleconnection persistence to MJO propagation is
396 consistent with Zheng and Chang (2019). During the transition of equatorial MJO events
397 from heating anomalies of one sign to the opposite sign, the forced extratropical response
398 will gradually change sign, which interfere destructively with the anomalies generated by
399 the previous phases and lead to a decay of MJO teleconnections. If the MJO is non-
400 propagating, destructive teleconnection signals cannot be generated later, which gives rise
401 to a longer persistence of teleconnections. Although opposite-sign heating anomalies may
402 be initiated afterwards over the Indian Ocean, they are usually very weak for the non-
403 propagating MJO events (Feng et al. 2015). The results above support the hypothesis that
404 the longer persistence of MJO teleconnections simulated by most of the current GCMs
405 (Part I) may be due to the exaggerated Maritime Continent barrier effect of the MJO in
406 models (Fig. 1).

407 *c. Impact of MJO propagation speed on teleconnection amplitude*

408 As discussed in section 3, a fast propagating MJO may lead to weaker teleconnections
409 than a slow propagating MJO (Bladé and Hartmann 1995; Yadav and Straus 2017; Goss
410 and Feldstein 2018; Zheng and Chang 2019). This influence is tested through an LBM

Accepted for publication in *Journal of Climate*. DOI 10.1175/JCLI-D-19-0865.1.

411 experiment by varying the speed of the propagating anomalous Q_1 from 5-day/phase
412 (phase speed at ~ 5 m/s, control run) to 4-day/phase (phase speed at ~ 6 m/s, *Fast_MJO*
413 run) and 6-day/phase (phase speed at ~ 4 m/s, *Slow_MJO* run). The MJO propagation will
414 thus last for 32 days for the *Fast_MJO* run (Fig. 7a) and 48 days for the *Slow_MJO* run
415 (Fig. 7b), which coincides approximately with the spread of model bias of the MJO period
416 (Fig. 2c). Phase 3 teleconnection in the *Fast_MJO* (average over model days 14-21
417 considering 4-day/phase) and *Slow_MJO* run (average over model days 18-27 considering
418 6-day/phase) are compared in Fig. 10. The extratropical response becomes stronger in the
419 *Slow_MJO* than that in the *Fast_MJO* run (Relative amplitude (T2): 1.12 vs. 0.86),
420 consistent with the relationship found in section 3. Because most GCMs have faster MJO
421 propagation and stronger MJO teleconnections than the observed, the LBM results (faster
422 MJO propagation induces weaker teleconnections) suggest that the bias of teleconnection
423 amplitude in GCMs is not directly attributed to biases in the MJO propagation speed or the
424 MJO impact is overpowered by the basic state impacts discussed below.

425 *d. Impact of jet characteristics on teleconnection amplitude and position*

426 Bias in the amplitude and position of the subtropical westerly jet may lead to bias in the
427 amplitude and position of MJO teleconnections (section 4). However, bias in the jet
428 amplitude is usually accompanied by bias in the jet position (section 4), thus obscuring
429 their independent impact on MJO teleconnections. To understand the independent impact
430 of jet amplitude, zonal extension, and meridional shift on MJO teleconnections, three sets
431 of paired experiments are carried out. Their corresponding basic states are derived from
432 models following the selection criteria: First, models with remarkable biases in B2 (jet
433 amplitude), B3 (zonal extension of the jet), or B4 (meridional shift of the jet) are selected

Accepted for publication in *Journal of Climate*. DOI 10.1175/JCLI-D-19-0865.1.

based on Fig. 6. Remarkable jet biases are defined as basic state metrics within the top 25% among models for B2 and B3, and bottom 25% for B4, given that models are generally biased to a stronger westerly jet (larger B2) with an eastward extension (larger B3) and/or a southward shift (smaller B4). Some models (e.g., IPSL-CM5A-LR and MRI-ESM1) are double/triple-counted. Hence, to isolate the impact of a certain jet bias, models with a remarkable bias in the other two jet categories are excluded. With these criteria, the basic state from ACCESS1-3 (Fig. 5c) is prescribed in the LBM to investigate the impact of the stronger jet on MJO teleconnections (*StrongU_BS* run). GFDL-ESM2M (Fig. 5k) is used to examine the impact of the eastward jet extension (*EastU_BS* run) on MJO teleconnections, and MIROC5 (Fig. 5o) used for the southward jet shift (*SouthU_BS* run). The opposite biases from the selected models are added to the observed climatology to analyze the opposite jet impacts on MJO teleconnections (Table 4). We use the model bias to test impacts of the basic state on MJO teleconnections instead of modifying the observed basic state directly because 1) understanding impacts of the model bias is the main focus of this study and 2) to maintain the geostrophic balance, it is hard to perturb one characteristic of the jet while keeping all other characteristics completely unchanged.

Mechanisms of the basic state impacts on MJO teleconnections are examined by examining the stationary wavenumber K_S on Mercator coordinates, which is obtained following Hoskins and Ambrizzi (1993):

$$K_S = a\left(\frac{\beta_M}{\overline{U}_M}\right)^{1/2},$$

where a is the Earth radius, $\overline{U}_M$ is the mean zonal wind divided by the cosine of latitude. β_M is equivalent to $\beta^* = \frac{\partial f}{\partial y} - \frac{\partial^2 \overline{u}}{\partial y^2}$ defined as the meridional gradient of absolute vorticity on a sphere multiplied by the cosine of latitude:

Accepted for publication in *Journal of Climate*. DOI 10.1175/JCLI-D-19-0865.1.

$$\beta_M = cos\varphi \frac{1}{a}\frac{\partial \zeta_a}{\partial \varphi} = \left[2\Omega - \left(\frac{1}{cos\varphi}\frac{\partial}{\partial \varphi}\right)^2 \left(\frac{cos^2\varphi \bar{U}_M}{a}\right)\right]\frac{cos^2\varphi}{a},$$

where ζ_a is the absolute vorticity, Ω is the rotation rate of the Earth. Model K_S is compared with observations in Fig. 11. White areas are where waves are dissipated since $\bar{U}_M < 0$. Black shadings denote regions where $\beta_M < 0$. According to the Rossby wave theory (Hoskins and Karoly 1981; Hoskins and Ambrizzi 1993), waves reflect at the turning latitude where zonal wavenumber k equals to K_S (thus meridional wavenumber $l = 0$) or where $\beta_M < 0$ (thus $l^2 < 0$), and refract toward regions with high K_S. As shown in observations (Fig. 11a), regions with $\beta_M < 0$ are at the poleward and equatorward sides of the subtropical westerly jet due to the strong meridional curvature ($\frac{\partial^2 \bar{u}}{\partial y^2}$) there, and the jet, where K_S is large, acts as a westerly waveguide. Thus the MJO-forced Rossby waves, especially those with zonal wavenumbers 3 and 4, propagate eastward along the jet and emanate at the jet exit region; Rossby waves with zonal wavenumbers 1 and 2 penetrate beyond the jet and propagate directly to the PNA region following K_S contours 1 and 2 (Seo and Lee 2017). A bias in β_M and K_S in a model can thus lead to biases in the position and propagation of MJO teleconnections.

Results of the sensitivity experiments (Fig. 12) are explained based on the above mechanisms. In a comparison of *StrongU_BS* (Fig. 12a) and *WeakU_BS* run (Fig. 12b), when the jet becomes stronger, MJO teleconnections tend to be stronger (T2 as 1.13) accordingly, and vice versa when the jet is weaker. This is consistent with ray theory (Hoskins and Karoly 1981) in that the energy (i.e., amplitude) of stationary Rossby waves is proportional to the speed of the mean zonal wind along a ray. The jet amplitude also seems to affect the east-west position of teleconnection patterns that a stronger jet leads to

Accepted for publication in *Journal of Climate*. DOI 10.1175/JCLI-D-19-0865.1.

479 an eastward shift in MJO teleconnections over the North Pacific (Fig. 12a). This is because
480 a stronger jet is associated with a stronger meridional curvature ($\frac{\partial^2 \overline{u}}{\partial y^2}$), thus a smaller β_M on
481 the poleward and equatorward sides of the jet (i.e., larger areas of $\beta_M < 0$ in ACCESS1-3,
482 Fig. 11b) compared to observations (Fig. 11a). Therefore, Rossby wave propagation may
483 be more confined to the westerly waveguide due to greater wave reflection (i.e., less
484 meridional wave penetration beyond the jet into the extratropics) until Rossby waves reach
485 the exit region. As a result, meridional propagation of Rossby waves into the extratropics
486 could occur further eastward in response to a stronger jet, illustrated by an eastward shift
487 in MJO teleconnections as shown in Fig. 12a. When the subtropical jet extends eastward
488 (*EastU_BS* vs. *WestU_BS* run, Figs. 12c and d), MJO teleconnections over the North
489 Pacific also tend to shift eastward (Fig. 12d) due to an eastward extension of the westerly
490 waveguide (Fig. 11c).

491 On the other hand, a southward jet shift (*SouthU_BS* run, Fig. 12e) leads to stronger
492 teleconnection amplitude (T2 as 1.41) than a northward jet shift (*NorthU_BS* run, Fig. 12f).
493 This is possibly because of an easier excitation of Rossby waves when the strong absolute
494 vorticity gradient in the jet is placed closer to the heat source and associated divergent
495 winds (Frederiksen and Webster 1988) (see the RWS in Fig. 7 of Part I). Although this
496 linear relationship is not found in GCMs (section 4), we found that among the 18 GCMs
497 that have stronger teleconnection amplitude, 12 of them have a southward shifted jet. The
498 southward jet shift also causes changes in the teleconnection pathway: teleconnections
499 propagate more zonally oriented (Fig. 12e) than those in response to the northward jet shift
500 (Fig. 12f), which is discerned as the cyclonic anomaly over Alaska extending southward in
501 the *SouthU_BS* run than that in the *NorthU_BS* run. This change in the teleconnection

Accepted for publication in *Journal of Climate*. DOI 10.1175/JCLI-D-19-0865.1.

pathway as a result of the meridional jet shift is also discussed in Henderson et al. (2017), which may be due to the difference in the position of the turning latitude. According to Seo and Lee (2017), MJO-forced Rossby waves consist of zonal wavenumbers 1 and 2 that penetrate to Alaska and zonal wavenumbers 3 and 4 that propagate more zonally oriented. This is consistent with the distribution of K_S (Fig. 11a), i.e., shorter waves reach their turning latitudes ($K_S = k$) at a lower latitude. Therefore, if K_S contours are located more equatorward, it is expected that teleconnections will propagate in a manner that is more zonally oriented as they would encounter their turning latitudes at a lower latitude. In MIROC5 (Fig. 11d), K_S 3 and 4 contours north of the jet exit region (~180°-120°W, 30°-60°N) are shifted equatorward compared to observations (Fig. 11a). As a result, the poleward propagating Rossby waves would turn at a lower latitude in response to a southward jet shift, leading to a more zonally oriented wave propagation, illustrated by a southward extension of Z500a over Alaska. The southward jet shift also leads to a westward shift in MJO teleconnections over the North Pacific (Fig. 12e), which contradicts the relationship found in GCMs that a southward jet shift is correlated with an eastward shift in MJO teleconnections (section 4). This discrepancy is possibly caused by two reasons. First, the LBM is based on the linear dynamics. When the jet shifts equatorward, assuming the meridional curvature ($\frac{\partial^2 \overline{u}}{\partial y^2}$) is not changed, only $\frac{\partial f}{\partial y}$ increases as the jet locates at a lower latitude with larger planetary vorticity gradient. β_M will thus increase on both sides of the jet as seen in Fig. 11d (i.e., smaller areas of $\beta_M < 0$ in MIROC5), which is more favorable for the poleward wave propagation occurring westward in the *SouthU_BS* run compared to the *NorthU_BS* run. Second, the negative relationship found in GCMs between B4 (meridional shift of the jet) and T3 (east-west position) is effectively

Accepted for publication in *Journal of Climate*. DOI 10.1175/JCLI-D-19-0865.1.

525 dominated by the impact from B2 (jet amplitude) which has a positive relationship with T3
526 and a negative relationship with B4. This is supported by the reduced partial correlation
527 (correlation at -0.21) between T3 and B4 when controlling the effect of B2.

528 The above basic state experiments suggest that the eastward shift in MJO
529 teleconnections simulated by current GCMs (Part I) can be attributed to the stronger and/or
530 eastward extended westerly jet (Figs. 6b and c) simulated by most models, and the stronger
531 teleconnection amplitude can be attributed to the stronger westerly jet and/or the southward
532 jet shift (Fig. 6d).

533

534 **6. Summary and discussion**

535 In Part I of this study that examined 29 GCMs, it was shown that models generally
536 produce MJO teleconnections with an eastward shift, larger amplitude, and longer
537 persistence compared to the observed counterparts. To quantify the impacts of the
538 simulated MJO and basic state on MJO teleconnections, various existing and newly-
539 developed MJO and basic state metrics are applied to the 29 GCMs in this study. Most
540 models simulate an MJO with weaker amplitude, faster propagation speed, and less
541 coherent eastward propagation than the observed. A majority of models produce a stronger
542 Pacific westerly jet with an eastward extension or southward shift relative to observations.
543 The above biases are significant at the 95% confidence level based on a two-tailed test of
544 differences between observations and the multi-model mean (not shown). By calculating
545 linear correlations between various metrics of MJO teleconnections, MJO characteristics,
546 and basic state characteristics, it is found that models that produce realistic MJO patterns
547 with a better and coherent eastward propagation generally produce more realistic

Accepted for publication in *Journal of Climate*. DOI 10.1175/JCLI-D-19-0865.1.

548 teleconnection patterns and persistence. Models with a stronger MJO tend to simulate
549 stronger MJO teleconnections with higher consistency between individual MJO events,
550 and longer persistence of patterns. Models with a slower MJO propagation produce
551 stronger MJO teleconnections. Compared to variations in MJO characteristics, the westerly
552 jet mainly influences the east-west position of MJO teleconnections. A stronger and/or
553 eastward-extended westerly jet can lead to an eastward shift in MJO teleconnections. In
554 addition, a stronger jet may lead to stronger MJO teleconnections. Although the above
555 relationships may not be valid for all models as the correlation is not perfect, they reveal
556 the potential sources of the teleconnection biases.

557 MJO and basic state impacts on MJO teleconnections are further investigated through
558 various LBM sensitivity experiments (Table 4) by changing the MJO propagation
559 characteristics and by isolating impacts from variations in jet amplitude and position.
560 Results indicate that 1) teleconnections generated in response to a non-propagating MJO
561 persist longer than for a propagating MJO; 2) a faster propagating MJO produces weaker
562 teleconnections than a more slowly propagating MJO; 3) a stronger and/or eastward-
563 extended jet leads to an eastward shift in MJO teleconnections; 4) MJO teleconnections are
564 stronger when the jet is stronger and/or shifts southward; 5) MJO teleconnections
565 propagate with a more zonally oriented pathway when the jet shifts southward.

566 Results in this study suggest that the longer persistence of MJO teleconnections found
567 in the 29 GCMs may be due to exaggerated Maritime Continent barrier effect of the MJO
568 in models. The eastward shift and larger amplitude of MJO teleconnections may be
569 attributed to biases in the jet. Therefore, to better represent MJO teleconnections, both the
570 MJO and basic state need to be accurately simulated.

Accepted for publication in *Journal of Climate*. DOI 10.1175/JCLI-D-19-0865.1.

571 This study provides a better understanding of the relative impact of MJO and basic state
572 characteristics on MJO teleconnections and the possible causes of biases in teleconnection
573 simulations. However, characteristics of the MJO differ from event to event and the
574 subtropical jet is also impacted by the MJO (Kang and Tziperman 2018). Interpretation is
575 further complicated by the fact that changes in MJO teleconnections can be a result of
576 various MJO or basic state influences. For example, a stronger MJO or less coherent MJO
577 propagation can both lead to longer teleconnection persistence, and biases in jet amplitude
578 and position can both lead to an east-west shift in teleconnections. The relative contribution
579 from such impacts of different MJO or basic state characteristics on the same
580 teleconnection bias merits further investigation.

581 The MJO and subtropical jet may be modulated by slowly varying basic state variability,
582 such as that caused by El Niño–Southern Oscillation (ENSO; Hendon et al. 1999;
583 Takahashi and Shirooka 2014; Henderson and Maloney 2018) or the Quasi-Biennial
584 Oscillation (QBO; Yoo and Son 2016; Wang et al. 2018b). The results found in this study
585 may therefore be influenced by the model ability to simulate the observed features of
586 interannual variability. In addition, the processes responsible for MJO teleconnections
587 include both linear and nonlinear effects (Bladé and Hartmann 1995; Lin and Brunet 2018).
588 The LBM used in this study has limitations in that it is based on linear dynamics, and
589 therefore may lead to oversimplified results. After the first week, the extratropical response
590 to the MJO becomes more nonlinear such that the response is asymmetric between the MJO
591 mirror phases (Lin and Brunet 2018), which may not be presented by the LBM. The
592 possible influence from nonlinearity will be examined in future work.
593

Accepted for publication in *Journal of Climate*. DOI 10.1175/JCLI-D-19-0865.1.

Acknowledgements

We would like to thank WGNE MJO Task Force members for stimulating discussions during the course of this study. We thank Dr. Xianan Jiang for providing the GASS/YoTC model data, Dr. Aneesh Subramanian for providing the ECMWF model data, Dr. Masahiro Watanabe for providing the LBM package, and Dr. Masato Mori for providing the code modifications for the LBM propagating heat source. JW was supported by NSF grant AGS-1652289, HK was supported by NSF grant AGS-1652289, NOAA MAPP grant NA16OAR4310070, and KMA R&D Program grant KMI2018-03110. DK was supported by the U.S. DOE RGMA program grant DE-SC0016223, NOAA CVP grant NA18OAR4310300, and NASA MAP grant 80NSSC17K0227. EDM was supported by NSF grant AGS-1841754, NOAA MAPP grants NA16OAR4310064 and NA18OAR4310268, and NOAA CVP grant NA18OAR4310299.

Accepted for publication in *Journal of Climate*. DOI 10.1175/JCLI-D-19-0865.1.

606 **References**

607 Adames, Á. F., and J. M. Wallace, 2014: Three-dimensional structure and evolution of the
608 MJO and its relation to the mean flow. *J. Atmos. Sci.*, **71**, 2007-2026,
609 doi:10.1175/JAS-D-13-0254.1.

610 Ahn, M.-S., D. Kim, K. R. Sperber, I.-S. Kang, E. Maloney, D. Waliser, and H. Hendon,
611 2017: MJO simulation in CMIP5 climate models: MJO skill metrics and process-
612 oriented diagnosis. *Climate Dyn.*, **49**, 4023-4045, doi:10.1007/s00382-017-3558-4.

613 Alaka Jr, G. J., and E. D. Maloney, 2012: The influence of the MJO on upstream precursors
614 to African easterly waves. *J. Climate*, **25,** 3219-3236, doi:10.1175/JCLI-D-11-
615 00232.1.

616 Bao, M., and D. L. Hartmann, 2014: The response to MJO-like forcing in a nonlinear
617 shallow-water model. *Geophys. Res. Lett.*, **41**, 1322-1328,
618 doi:10.1002/2013GL057683.

619 Bladé, I., and D. L. Hartmann, 1995: The linear and nonlinear extratropical response of the
620 atmosphere to tropical intraseasonal heating. *J. Atmos. Sci.*, **52**, 4448-4471,
621 doi:10.1175/1520-0469(1995)052<4448:TLANER>2.0.CO;2.

622 Cassou, C., 2008: Intraseasonal interaction between the Madden–Julian oscillation and the
623 North Atlantic Oscillation. *Nature*, **455**, 523-527.

624 Davini, P., and Coauthors, 2017: Climate SPHINX: evaluating the impact of resolution and
625 stochastic physics parameterisations in the EC-Earth global climate model. *Geosci.*
626 *Model Dev.*, **10,** 1383-1402, doi:10.5194/gmd-10-1383-2017.

Accepted for publication in *Journal of Climate*. DOI 10.1175/JCLI-D-19-0865.1.

627 Dee, D. P., and Coauthors, 2011: The ERA-Interim reanalysis: Configuration and
628 performance of the data assimilation system. *Quart. J. Roy. Meteor. Soc.*, **137**, 553–
629 597, doi:10.1002/qj.828.
630 Deng, Y., and T. Jiang, 2011: Intraseasonal modulation of the North Pacific storm track by
631 tropical convection in boreal winter. *J. Climate*, **24**, 1122-1137,
632 doi:10.1175/2010JCLI3676.1.
633 Duchon, C. E., 1979: Lanczos filtering in one and two dimensions. *J. Appl. Meteor.*
634 *Climatol.*, **18,** 1016-1022.
635 Duffy, P., and Coauthors, 2003: High-resolution simulations of global climate, part 1:
636 present climate. *Climate Dyn.*, **21**, 371-390.
637 Feng, J., T. Li, and W. Zhu, 2015: Propagating and nonpropagating MJO events over
638 Maritime Continent. *J. Climate*, **28,** 8430-8449.
639 Frederiksen, J. S., and P. J. Webster, 1988: Alternative theories of atmospheric
640 teleconnections and low‐frequency fluctuations. *Rev. Geophys.*, **26**, 459-494.
641 Gong, H., L. Wang, W. Chen, R. Wu, K. Wei, and X. Cui, 2014: The climatology and
642 interannual variability of the East Asian winter monsoon in CMIP5 models. *J.*
643 *Climate*, **27,** 1659-1678, doi:10.1175/JCLI-D-13-00039.1.
644 Goss, M., and S. B. Feldstein, 2018: Testing the sensitivity of the extratropical response to
645 the location, amplitude, and propagation speed of tropical convection. *J. Atmos.*
646 *Sci.*, **75,** 639-655.
647 Hendon, H. H., C. Zhang, and J. D. Glick, 1999: Interannual variation of the Madden-
648 Julian oscillation during austral summer. *J. Climate*, **12,** 2538-2550.

Accepted for publication in *Journal of Climate*. DOI 10.1175/JCLI-D-19-0865.1.

649 Henderson, S. A., E. D. Maloney, and E. A. Barnes, 2016: The influence of the Madden–
650 Julian oscillation on Northern Hemisphere winter blocking. *J. Climate*, **29**, 4597–
651 4616, doi:10.1175/JCLI-D-15-0502.1.
652 ——, ——, and S.-W. Son, 2017: Madden–Julian oscillation Pacific teleconnections: The
653 impact of the basic state and MJO representation in general circulation models. *J.*
654 *Climate*, **30**, 4567-4587, doi:10.1175/JCLI-D-16-0789.1.
655 ——, and ——, 2018: The impact of the Madden–Julian oscillation on high-latitude winter
656 blocking during El Niño–Southern Oscillation events. *J. Climate*, **31,** 5293-5318.
657 ——, D. J. Vimont, and M. Newman, 2019: "The critical role of non-normality in
658 partitioning tropical and extratropical contributions to PNA growth". *J. Climate*,
659 submitted.
660 Horel, J. D., and J. M. Wallace, 1981: Planetary-scale atmospheric phenomena associated
661 with the Southern Oscillation. *Mon. Wea. Rev.*, **109**, 813-829.
662 Hoskins, B. J., and D. J. Karoly, 1981: The steady linear response of a spherical atmosphere
663 to thermal and orographic forcing. *J. Atmos. Sci.*, **38**, 1179-1196,
664 doi:10.1175/1520-0469(1981)038<1179:TSLROA>2.0.CO;2.
665 ——, and T. Ambrizzi, 1993: Rossby wave propagation on a realistic longitudinally
666 varying flow. *J. Atmos. Sci.*, **50,** 1661-1671.
667 Jiang, X., and Coauthors, 2015: Vertical structure and physical processes of the Madden‐
668 Julian oscillation: Exploring key model physics in climate simulations. *J. Geophys.*
669 *Res. Atmos.*, **120**, 4718-4748, doi:10.1002/2014JD022375.
670 Kang, W., and E. Tziperman, 2018: The MJO‐SSW Teleconnection: Interaction Between
671 MJO‐Forced Waves and the Midlatitude Jet. *Geophys. Res. Lett.*, **45**, 4400-4409.

Accepted for publication in *Journal of Climate*. DOI 10.1175/JCLI-D-19-0865.1.

672 Karoly, D., 1983: Rossby wave propagation in a barotropic atmosphere. *Dyn. Atmos.*
673 *Oceans*, **7**, 111–125, doi:10.1016/0377-0265(83)90013-1.
674 Kim, D., and Coauthors, 2009: Application of MJO simulation diagnostics to climate
675 models. *J. Climate*, **22,** 6413-6436, doi:10.1175/2009JCLI3063.1.
676 ——, J.-S. Kug, and A. H. Sobel, 2014a: Propagating versus nonpropagating Madden–
677 Julian oscillation events. *J. Climate*, **27,** 111-125.
678 ——, and Coauthors, 2014b: Process-oriented MJO simulation diagnostic: Moisture
679 sensitivity of simulated convection. *J. Climate*, **27**, 5379–5395, doi:10.1175/JCLI-
680 D-13-00497.1.
681 Lappen, C.-L., and C. Schumacher, 2012: Heating in the tropical atmosphere: what level
682 of detail is critical for accurate MJO simulations in GCMs? *Climate Dyn.*, **39,** 2547-
683 2568.
684 Liebmann, B., and C. A. Smith, 1996: Description of a complete (interpolated) outgoing
685 longwave radiation dataset. *Bull. Amer. Meteor. Soc.*, **77,** 1275-1277,
686 Lin, H., G. Brunet, and J. Derome, 2009: An observed connection between the North
687 Atlantic Oscillation and the Madden–Julian oscillation. *J. Climate*, **22,** 364-380,
688 doi:10.1175/2008JCLI2515.1.
689 ——, and ——, 2018: Extratropical response to the MJO: Nonlinearity and sensitivity to
690 the initial state. *J. Atmos. Sci.*, **75,** 219-234, doi:10.1175/JAS-D-17-0189.1.
691 Madden, R. A., and P. Julian, 1971: Detection of a 40–50 day oscillation in the zonal wind
692 in the tropical Pacific. *J. Atmos. Sci.*, **28**, 702–708, doi:10.1175/1520-
693 0469(1971)028,0702:DOADOI.2.0.CO;2.

Accepted for publication in *Journal of Climate*. DOI 10.1175/JCLI-D-19-0865.1.

694 ——, and ——, 1972: Description of a global-scale circulation cells in the tropics with a
695 40–50 day period. *J. Atmos. Sci.*, **29**, 1109–1123, doi:10.1175/1520-
696 0469(1972)029,1109:DOGSCC.2.0.CO;2.
697 Mori, M., and M. Watanabe, 2008: The growth and triggering mechanisms of the PNA: A
698 MJO-PNA coherence. *J. Meteor. Soc. Japan*, **86**, 213–236,
699 doi:10.2151/jmsj.86.213.
700 Mundhenk, B. D., E. A. Barnes, and E. D. Maloney, 2016: All-season climatology and
701 variability of atmospheric river frequencies over the North Pacific. *J. Climate*, **29,**
702 4885-4903, doi:10.1175/JCLI-D-15-0655.1.
703 Rui, H., and B. Wang, 1990: Development characteristics and dynamic structure of tropical
704 intraseasonal convection anomalies. *J. Atmos. Sci.*, **47,** 357-379.
705 Sardeshmukh, P. D., and B. J. Hoskins, 1988: The generation of global rotational flow by
706 steady idealized tropical divergence. *J. Atmos. Sci.*, **45**, 1228-1251,
707 doi:10.1175/1520-0469(1988)045<1228:TGOGRF>2.0.CO;2.
708 Seo, K.-H., and H.-J. Lee, 2017: Mechanisms for a PNA-Like Teleconnection Pattern in
709 Response to the MJO. *J. Atmos. Sci.*, **74**, 1767-1781, doi:10.1175/JAS-D-16-0343.1.
710 Simmons, A., J. Wallace, and G. Branstator, 1983: Barotropic wave propagation and
711 instability, and atmospheric teleconnection patterns. *J. Atmos. Sci.*, **40,** 1363-1392,
712 doi:10.1175/1520-0469(1983)040<1363:BWPAIA>2.0.CO;2.
713 Sperber, K. R., and D. Kim, 2012: Simplified metrics for the identification of the Madden–
714 Julian oscillation in models. *Atmos. Sci. Lett.*, **13,** 187-193, doi:10.1002/asl.378.

Accepted for publication in *Journal of Climate*. DOI 10.1175/JCLI-D-19-0865.1.

715 Stan, C., D. M. Straus, J. S. Frederiksen, H. Lin, E. D. Maloney, and C. Schumacher, 2017:
716 Review of tropical‐extratropical teleconnections on intraseasonal time scales. *Rev.*
717 *Geophys.*, **55**, 902-937, doi:10.1002/2016RG000538.
718 ——, and ——, 2019: The impact of cloud representation on the sub-seasonal forecast of
719 atmospheric teleconnections and preferred circulation regimes in the Northern
720 Hemisphere. *Atmos*. *Ocean*, doi:10.1080/07055900.2019.1590178.
721 Takahashi, C., and R. Shirooka, 2014: Storm track activity over the North Pacific
722 associated with the Madden-Julian Oscillation under ENSO conditions during
723 boreal winter. *J. Atmos. Sci.*, **119,** 10,663-10,683, doi:10.1002/2014JD021973.
724 Taylor, K. E., 2001: Summarizing multiple aspects of model performance in a single
725 diagram. *J. Geophys. Res. Atmos.*, **106,** 7183-7192, doi:10.1029/2000JD900719.
726 ——, R. J. Stouffer, and G. A. Meehl, 2012: An overview of CMIP5 and the experiment
727 design. *Bull. Amer. Meteor. Soc.*, **93**, 485–498, doi:10.1175/BAMS-D-11-00094.1.
728 Tseng, K.-C., E. Maloney, and E. Barnes, 2019: The Consistency of MJO Teleconnection
729 Patterns: An Explanation Using Linear Rossby Wave Theory. *J. Climate*, **32,** 531-
730 548.
731 Waliser, D., and Coauthors, 2009: MJO simulation diagnostics. *J. Climate*, **22,** 3006-3030,
732 doi:10.1175/2008JCLI2731.1.
733 Wang, J., H. M. Kim, E. K. Chang, and S. W. Son, 2018a: Modulation of the MJO and
734 North Pacific Storm Track Relationship by the QBO. *J. Geophys. Res. Atmos.*, **123**,
735 3976- 3992, doi:10.1029/2017JD027977.
736 ——, ——, and ——, 2018b: Interannual modulation of Northern Hemisphere winter
737 storm tracks by the QBO. *Geophys. Res. Lett.*, **45,** 2786-2794.

Accepted for publication in *Journal of Climate*. DOI 10.1175/JCLI-D-19-0865.1.

738 ——, ——, D. Kim, S. A. Henderson, C. Stan, and E. D. Maloney, 2019: MJO
739 teleconnections over the PNA region in climate models. Part I: Performance- and
740 process-based skill metrics, *J. Climate*
741 Watanabe, M., and M. Kimoto, 2000: Atmosphere-ocean thermal coupling in the North
742 Atlantic: A positive feedback. *Quart. J. Roy. Meteor. Soc.*, **126**, 3343–3369,
743 doi:10.1002/qj.49712657017.
744 Wheeler, M. C., and H. H. Hendon, 2004: An all-season realtime multivariate MJO index:
745 Development of an index for monitoring and prediction. *Mon. Wea. Rev.*, **132**,
746 1917–1932, doi:10.1175/1520-0493(2004)132,1917:AARMMI.2.0.CO;2.
747 Winters, A. C., D. Keyser, and L. F. Bosart, 2019: The Development of the North Pacific
748 Jet Phase Diagram as an Objective Tool to Monitor the State and Forecast Skill of
749 the Upper-Tropospheric Flow Pattern. *Weather Forecast.,* **34,** 199-219.
750 Yadav, P., and D. M. Straus, 2017: Circulation response to fast and slow MJO episodes.
751 *Mon. Weather Rev.*, **145**, 1577-1596, doi:10.1175/MWR-D-16-0352.1.
752 Yanai, M., S. Esbensen, and J.-H. Chu, 1973: Determination of bulk properties of tropical
753 cloud clusters from large-scale heat and moisture budgets. *J. Atmos. Sci.*, **30**, 611–
754 627, doi:10.1175/1520-0469(1973)030,0611:DOBPOT.2.0.CO;2.
755 Yoo, C., S. Park, D. Kim, J.-H. Yoon, and H.-M. Kim, 2015: Boreal winter MJO
756 teleconnection in the Community Atmosphere Model version 5 with the unified
757 convection parameterization. *J. Climate*, **28**, 8135–8150, doi:10.1175/JCLI-D-15-
758 0022.1.

Accepted for publication in *Journal of Climate*. DOI 10.1175/JCLI-D-19-0865.1.

759 ——, and S. W. Son, 2016: Modulation of the boreal wintertime Madden- Julian
760 oscillation by the stratospheric quasi- biennial oscillation. *Geophys. Res. Lett.*, **43,**
761 1392-1398.
762 Zhang, C., and Coauthors, 2006: Simulations of the Madden–Julian oscillation in four pairs
763 of coupled and uncoupled global models. *Climate Dyn.*, **27,** 573-592,
764 doi:10.1007/s00382-006-0148-2.
765 Zheng, C., and E. Kar-Man Chang, H.-M. Kim, M. Zhang, and W. Wang, 2018: Impacts
766 of the Madden–Julian Oscillation on Storm-Track Activity, Surface Air
767 Temperature, and Precipitation over North America. *J. Climate*, **31,** 6113-6134.
768 ——, and ——, 2019: The role of MJO propagation, lifetime, and intensity on modulating
769 the temporal evolution of the MJO extratropical response. *J. Geophys. Res. Atmos.*,
770 **124**.
771 Zhou, S., M. L'Heureux, S. Weaver, and A. Kumar, 2012: A composite study of the MJO
772 influence on the surface air temperature and precipitation over the continental
773 United States. *Climate Dyn.*, **38,** 1459-1471.
774

Accepted for publication in *Journal of Climate*. DOI 10.1175/JCLI-D-19-0865.1.

775 Table list:

776 Table 1. Description of CMIP5 (#1-22), GASS/YoTC (#23-28), and ECMWF (#29)
777 models. Models in bold are 12 "good" MJO propagation models selected based on
778 MJO propagation skill (M1).

779 Table 2. Correlations between MJO teleconnection and MJO metrics calculated across all
780 models that exceed 90% confidence level based on a two-tailed test. (T1) Pattern
781 CC, (T2) Relative amplitude, (T4) Intra-phase pattern consistency (IPC), (T6)
782 Pattern CC of RWS, (T5) Persistence. (M1) MJO propagation skill, (M2)
783 Coherency, (M3) Period, (M4) OLR pattern CC, (M5) OLR amplitude.
784 Correlations are the average over all phases, except T5 which is the average of
785 phases 3 and 7. Correlations with an underline denote the results after removing the
786 outlier model HadGEM2-AO from calculation (results for all models are shown in
787 parenthesis).

788 Table 3. Correlations between MJO teleconnection and basic state metrics that exceed 90%
789 confidence level based on a two-tailed test. (T1) Pattern CC, (T2) Relative
790 amplitude, (T3) East-west position. (B1) RMSE, (B2) Jet amplitude, (B3) Zonal
791 extension of the jet, (B4) Meridional shift of the jet. Correlation between B1 and
792 T1 with an underline denotes the result based on 8 models with RMSE > 4.
793 Correlation between B2 and T2 with an underline represents the result after
794 removing the outlier model HadGEM2-AO from calculation. For these correlations,
795 results for all models are shown in parenthesis.

796 Table 4. Description of LBM experiments with a 50 day integration.

797

798

Accepted for publication in *Journal of Climate*. DOI 10.1175/JCLI-D-19-0865.1.

Figure List:

FIG. 1. Lead-lag composites of 10°S-10°N averaged (a) observed and (b-dd) modeled 25-90-day filtered OLR anomalies (unit: W m^{-2}) against convection averaged over the eastern Indian Ocean (75°-85°E, 5S°-5°N) with standard deviation less than -1.

FIG. 2. (a) MJO propagation skill (M1), (b) coherency (M2), and (c) period (M3) for observations (closed circles) and each model (open circles). Solid lines represent the multi-model mean. Dashed line in (a) denotes the threshold (correlation at 0.75) of "good" MJO propagation models.

FIG. 3. Wavenumber-frequency power spectra of 10°S–10°N averaged OLR (unit: W^2 m^{-4} per frequency interval per wavenumber interval) for (a) observations and (b-h) models. Power spectrum is calculated for each year and then averaged over all years. Dotted lines are drawn at frequencies corresponding to 30 and 80 days. The red box in (a) is the band where period (M3) is calculated.

FIG. 4. Taylor diagram of OLR pattern CC (M4) and OLR amplitude (M5) for MJO phase 3 (red square) and 7 (blue triangle). The distance between each model and the reference point "REF" indicates the root-mean-square error (RMSE).

FIG. 5. Climatology of U250 (contour interval: 10 m s^{-1} starting from 20 m s^{-1}) in (a) observations and (b-dd) models. Shading denotes the model biases, defined as the difference between the modeled and observed U250. Dotted areas indicate significant biases exceeding the 95% confidence level according to the two-tailed Student's t-test. Black box in (a) represents the region over 100°E-120°W, 10°-60°N.

Accepted for publication in *Journal of Climate*. DOI 10.1175/JCLI-D-19-0865.1.

FIG. 6. (a) RMSE (B1), (b) jet amplitude (B2), (c) zonal extension of the jet (B3), and (d) meridional shift of the jet (B4) for observations (closed circles) and each model (open circles). Solid lines represent the multi-model mean.

FIG. 7. The propagating MJO forcing used in LBM control run (shading, average over 10°S-10°N) and in the (a) *Fast_MJO* and (b) *Slow_MJO* runs (contour, interval: 0.2 K day^{-1}).

FIG. 8. (a) Phase 3 teleconnection in the LBM and the (b) observational reference (shading). Contour in (a) is the 1000- to 200-hPa averaged anomalous observational Q_1 for MJO phase 3 (average over model days 11-15): green (brown) represents MJO heating (cooling) with interval of 0.4 K day^{-1}. Contour in (b) is the composite of OLR anomaly over days in MJO phase 3: green (brown) represents enhanced (suppressed) MJO convection with interval of 10 W m^{-2}.

FIG. 9. Pattern CC between phase 3 teleconnection (i.e., Fig. 7a) and five-day running average of Z500a over the PNA region in the control run (black line). Red line is similar to black line but for the *Nonprop_MJO* run. Persistence is defined as number of days that pattern CC being larger than 0.5 (dashed line).

FIG. 10. Phase 3 teleconnection (shading) in the (a) *Fast_MJO* and (b) *Slow_MJO* runs. Contours are the difference from the control run (interval: 1 m). Values on the top right are MJO teleconnection metric T2 (Relative amplitude). T2 larger (smaller) than 1 indicates stronger (weaker) response than the control run.

Accepted for publication in *Journal of Climate*. DOI 10.1175/JCLI-D-19-0865.1.

841 FIG. 11. Stationary wavenumber K_S derived from climatological U250 on Mercator
842 coordinates. Black areas are where meridional gradient of absolute vorticity β_M is
843 negative. Regions of easterly zonal winds are in white.

844 FIG. 12. Same as Fig. 9 except for the (a) *StrongU_BS*, (b) *WeakU_BS*, (c) *EastU_BS*, (d)
845 *WestU_BS*, (e) *SouthU_BS*, and (f) *NorthU_BS* runs (contour interval: 2 m).
846 Anomalous Q_1 used in these experiments are the same with the control run, i.e., the
847 observational eastward propagating Q_1.

Accepted for publication in *Journal of Climate*. DOI 10.1175/JCLI-D-19-0865.1.

848 Table 1. Description of CMIP5 (#1-22), GASS/YoTC (#23-28), and ECMWF (#29)
849 models. Models in bold are 12 "good" MJO propagation models selected based on
850 MJO propagation skill (M1).

	Model	Modeling Center	Institution
1	ACCESS1-0	CSIRO-BOM	CSIRO (Commonwealth Scientific and Industrial Research Organization), and BOM (Bureau of Meteorology), Australia
2	ACCESS1-3		
3	CanESM2	CCCma	Canadian Centre for Climate Modelling and Analysis, Canada
4	CMCC-CESM	CMCC	Centro Euro-Mediterraneo per I Cambiamenti Climatici, Italy
5	CMCC-CM		
6	CMCC-CMS		
7	**CNRM-CM5**	CNRM-CERFACS	Centre National de Recherches Meteorologiques / Centre Europeen de Recherche et Formation Avancees en Calcul Scientifique, France
8	**GFDL-CM3**	NOAA GFDL	Geophysical Fluid Dynamics Laboratory, USA
9	GFDL-ESM2G		
10	GFDL-ESM2M		
11	HadGEM2-AO	MOHC	Met Office Hadley Centre, UK
12	HadGEM2-CC		
13	IPSL-CM5A-LR	IPSL	Institut Pierre-Simon Laplace, France
14	**MIROC5**	MIROC	Atmosphere and Ocean Research Institute (The University of Tokyo), National Institute for Environmental Studies, and Japan Agency for Marine-Earth Science and Technology, Japan
15	MIROC-ESM		
16	MIROC-ESM-CHEM		
17	MPI-ESM-LR	MPI-M	Max Planck Institute for Meteorology, Germany
18	MPI-ESM-MR		
19	MPI-ESM-P		

Accepted for publication in *Journal of Climate*. DOI 10.1175/JCLI-D-19-0865.1.

20	**MRI-CGCM3**	MRI	Meteorological Research Institute, Japan
21	**MRI-ESM1**		
22	**NorESM1-M**	NCC	Norwegian Climate Centre
23	**GISS-E2**	NASA GISS	NASA Goddard Institute for Space Studies
24	**MRI-AGCM3**	MRI	Meteorological Research Institute, Japan
25	**SPCAM3**		Colorado State University
26	**SPCCSM3**		George Mason University
27	**TAMU-CAM4**		Texas A&M University
28	NCAR-CAM5	NCAR	National Center for Atmospheric Research
29	**ECMWF**	ECMWF	European Centre for Medium-Range Weather Forecasts

851

Accepted for publication in *Journal of Climate*. DOI 10.1175/JCLI-D-19-0865.1.

852 Table 2. Correlations between MJO teleconnection and MJO metrics calculated across all
853 models that exceed 90% confidence level based on a two-tailed test. (T1) Pattern
854 CC, (T2) Relative amplitude, (T4) Intra-phase pattern consistency (IPC), (T6)
855 Pattern CC of RWS, (T5) Persistence. (M1) MJO propagation skill, (M2)
856 Coherency, (M3) Period, (M4) OLR pattern CC, (M5) OLR amplitude.
857 Correlations are the average over all phases, except T5 which is the average of
858 phases 3 and 7. Correlations in bold text denote the results after removing the outlier
859 model HadGEM2-AO from calculation (results for all models are shown in
860 parenthesis).

	T1 (pattern)	T2 (amplitude)	T4 (IPC)	T6 (RWS pattern)	$T5_{p3\&7}$ (persistence)
M1 (propagation)	0.36			0.34	-0.35
M2 (coherency)	0.56			0.42	-0.56
M3 (period)		**0.53** (*0.23*)			
M4 (pattern)	0.58			0.61	
M5 (amplitude)		**0.61** (*0.25*)	0.45		0.37

861

Accepted for publication in *Journal of Climate*. DOI 10.1175/JCLI-D-19-0865.1.

862 Table 3. Correlations between MJO teleconnection and basic state metrics that exceed 90%
863 confidence level based on a two-tailed test. (T1) Pattern CC, (T2) Relative
864 amplitude, (T3) East-west position. (B1) RMSE, (B2) Jet amplitude, (B3) Zonal
865 extension of the jet, (B4) Meridional shift of the jet. Correlation between B1 and
866 T1 in bold text denotes the result based on 8 models with RMSE > 4. Correlation
867 between B2 and T2 in bold text represents the result after removing the outlier
868 model HadGEM2-AO from calculation. For these correlations, results for all
869 models are shown in parenthesis.

	T1 (pattern)	T2 (amplitude)	T3 (east-west position)
B1 (RMSE)	**-0.83** (*-0.05*)		0.56
B2 (amplitude)		**0.36** (*0.13*)	0.58
B3 (zonal extension)			0.55
B4 (meridional shift)			-0.53

870

Accepted for publication in *Journal of Climate*. DOI 10.1175/JCLI-D-19-0865.1.

871 Table 4. Description of LBM experiments with a 50 day integration.

Experiments		MJO	Basic state (BS)
Control run		Observational (Obs) Q_1 propagating eastward from phase 1 to 8 with speed at 5-day/phase	Obs Oct-Mar climatology over period of 1979-2017
MJO runs	*Nonprop_MJO*	Obs Q_1 set to be stationary after reaching phase 4	Same as the control run
	Fast_MJO	Obs Q_1 propagating with speed at 4-day/phase	
	Slow_MJO	Obs Q_1 propagating with speed at 6-day/phase	
BS runs	*StrongU_BS*	Same as the control run	ACCESS1-3
	WeakU_BS		Obs climatology plus opposite model bias of ACCESS1-3
	EastU_BS		GFDL-ESM2M
	WestU_BS		Obs climatology plus opposite model bias of GFDL-ESM2M
	SouthU_BS		MIROC5
	NorthU_BS		Obs climatology plus opposite model bias of MIROC5

872

Accepted for publication in *Journal of Climate*. DOI 10.1175/JCLI-D-19-0865.1.

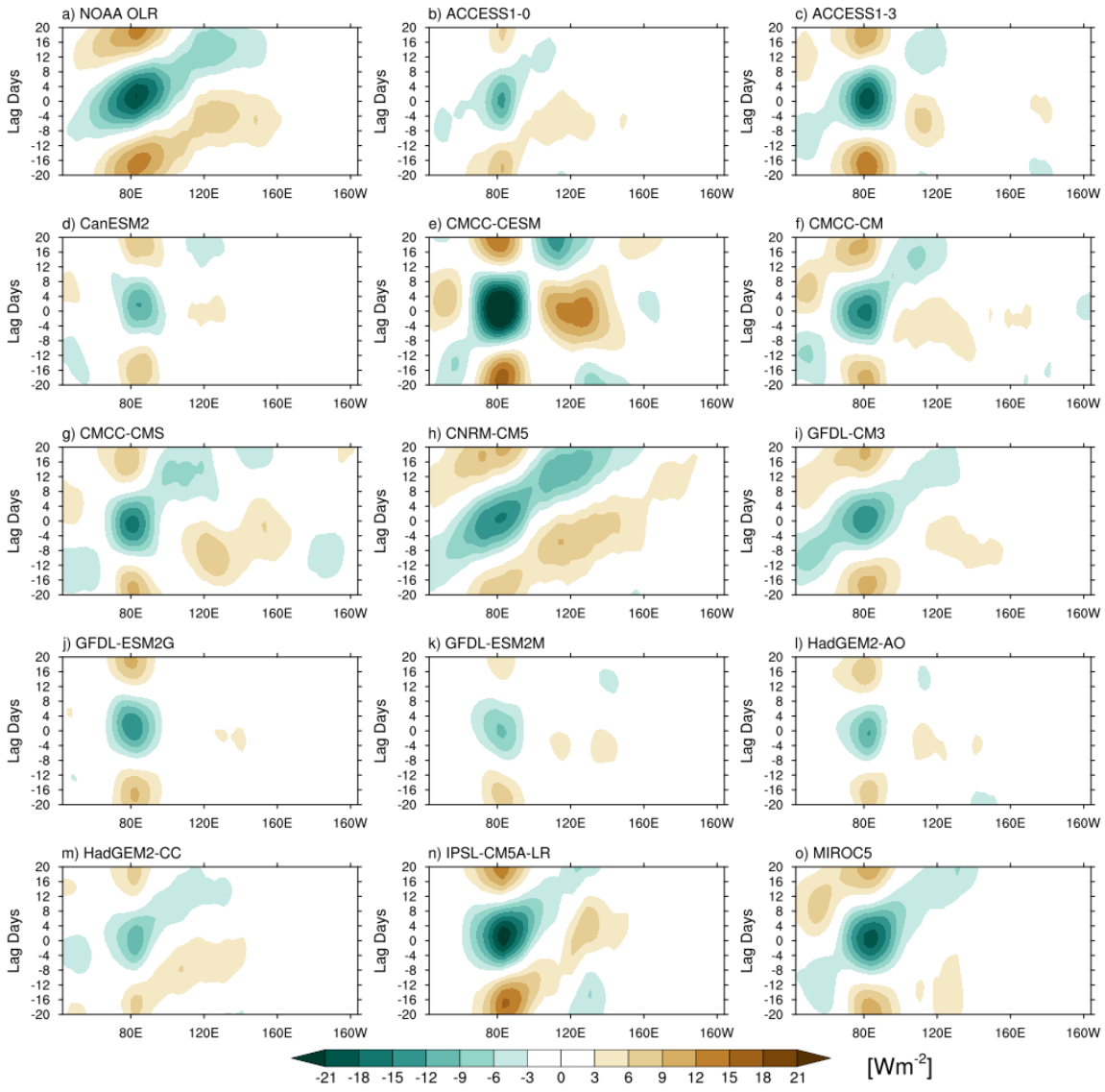

873

874 FIG. 1. Lead-lag composites of 10°S-10°N averaged (a) observed and (b-dd) modeled 25-
875 90-day filtered OLR anomalies (unit: W m^{-2}) against convection averaged over the
876 eastern Indian Ocean (75°-85°E, 5S°-5°N) with standard deviation less than -1.

Accepted for publication in *Journal of Climate*. DOI 10.1175/JCLI-D-19-0865.1.

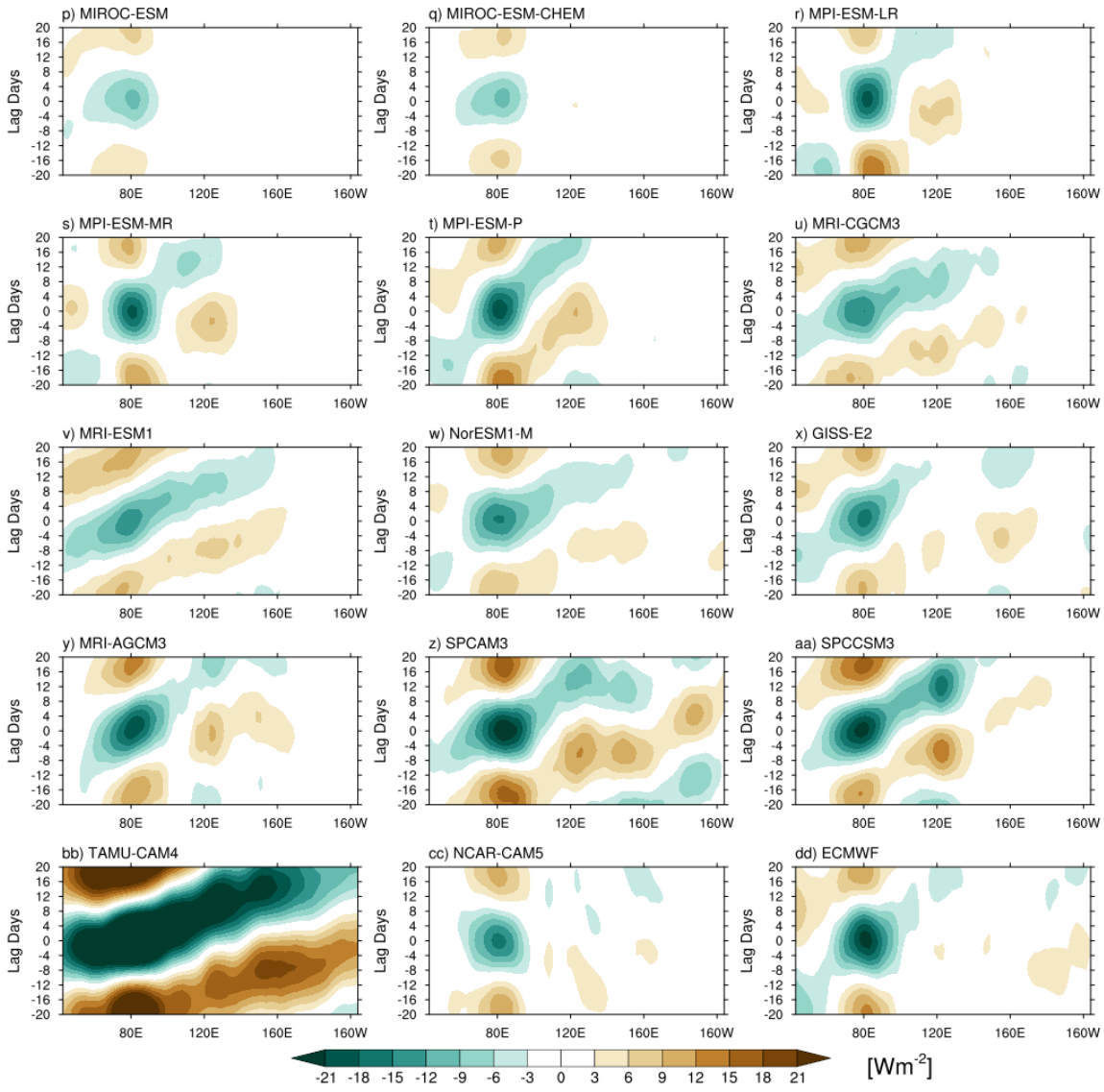

877

878 FIG. 1. (Continued).

Accepted for publication in *Journal of Climate*. DOI 10.1175/JCLI-D-19-0865.1.

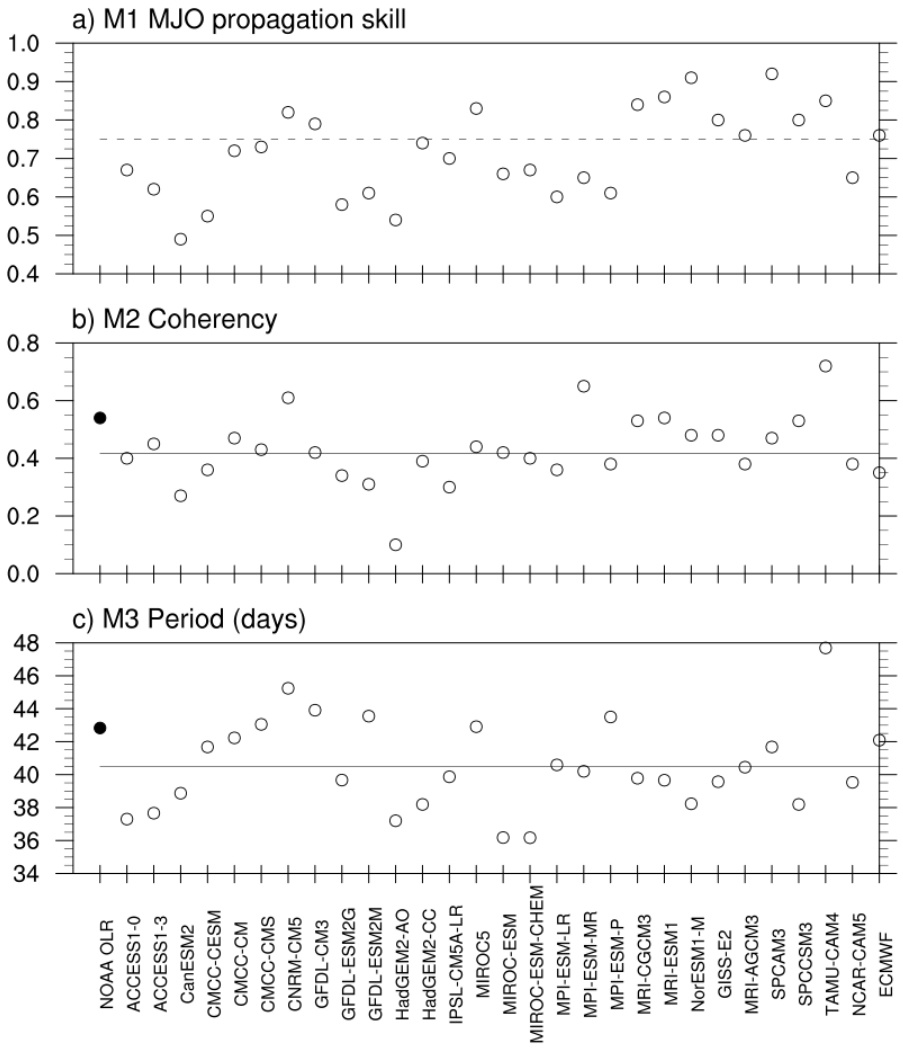

879

880 FIG. 2. (a) MJO propagation skill (M1), (b) coherency (M2), and (c) period (M3) for
881 observations (closed circles) and each model (open circles). Solid lines represent
882 the multi-model mean. Dashed line in (a) denotes the threshold (correlation at 0.75)
883 of "good" MJO propagation models.

Accepted for publication in *Journal of Climate*. DOI 10.1175/JCLI-D-19-0865.1.

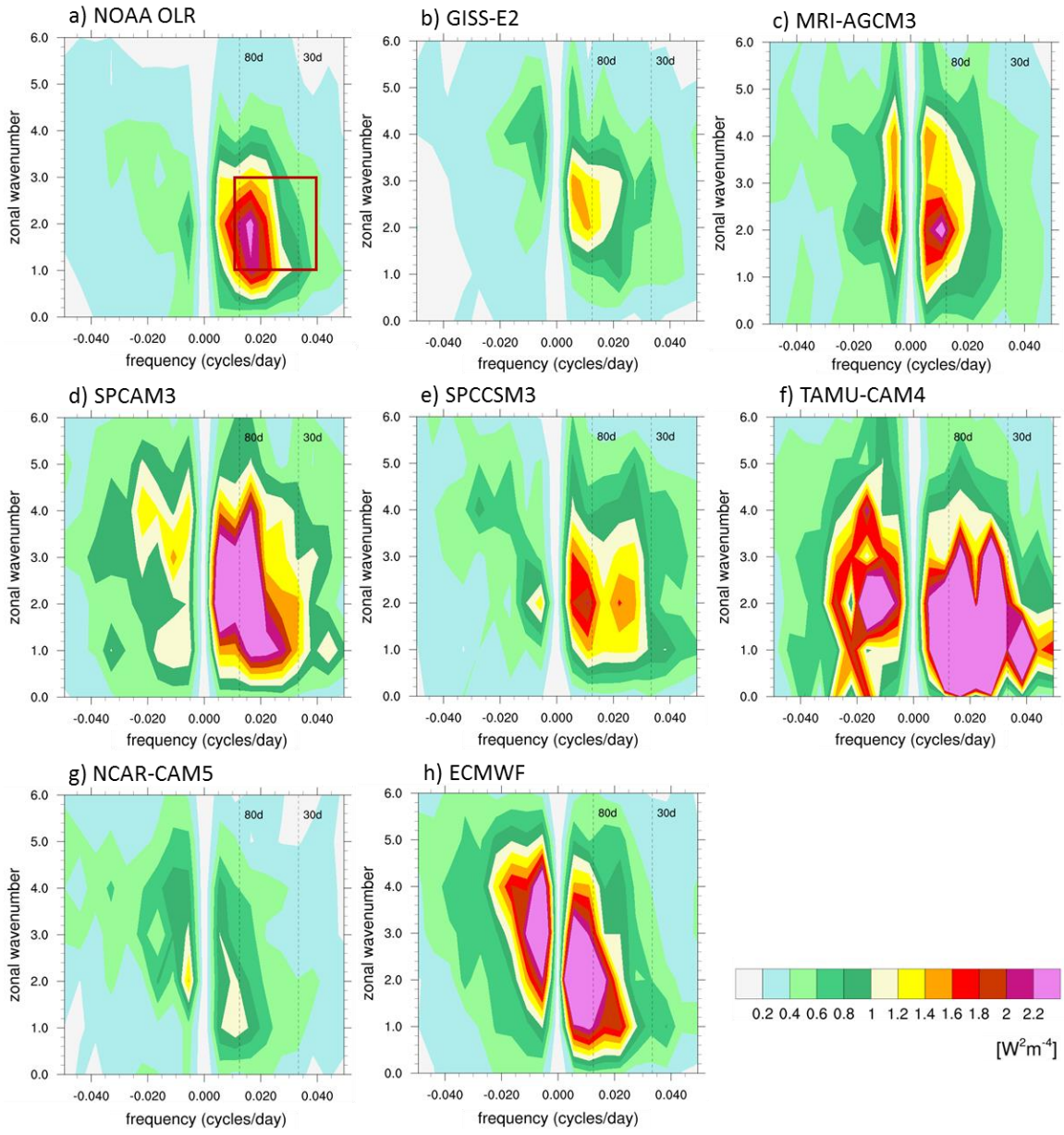

FIG. 3. Wavenumber-frequency power spectra of 10°S–10°N averaged OLR (unit: $W^2\ m^{-4}$ per frequency interval per wavenumber interval) for (a) observations and (b-h) models. Power spectrum is calculated for each year and then averaged over all years. Dotted lines are drawn at frequencies corresponding to 30 and 80 days. The red box in (a) is the band where period (M3) is calculated.

Accepted for publication in *Journal of Climate*. DOI 10.1175/JCLI-D-19-0865.1.

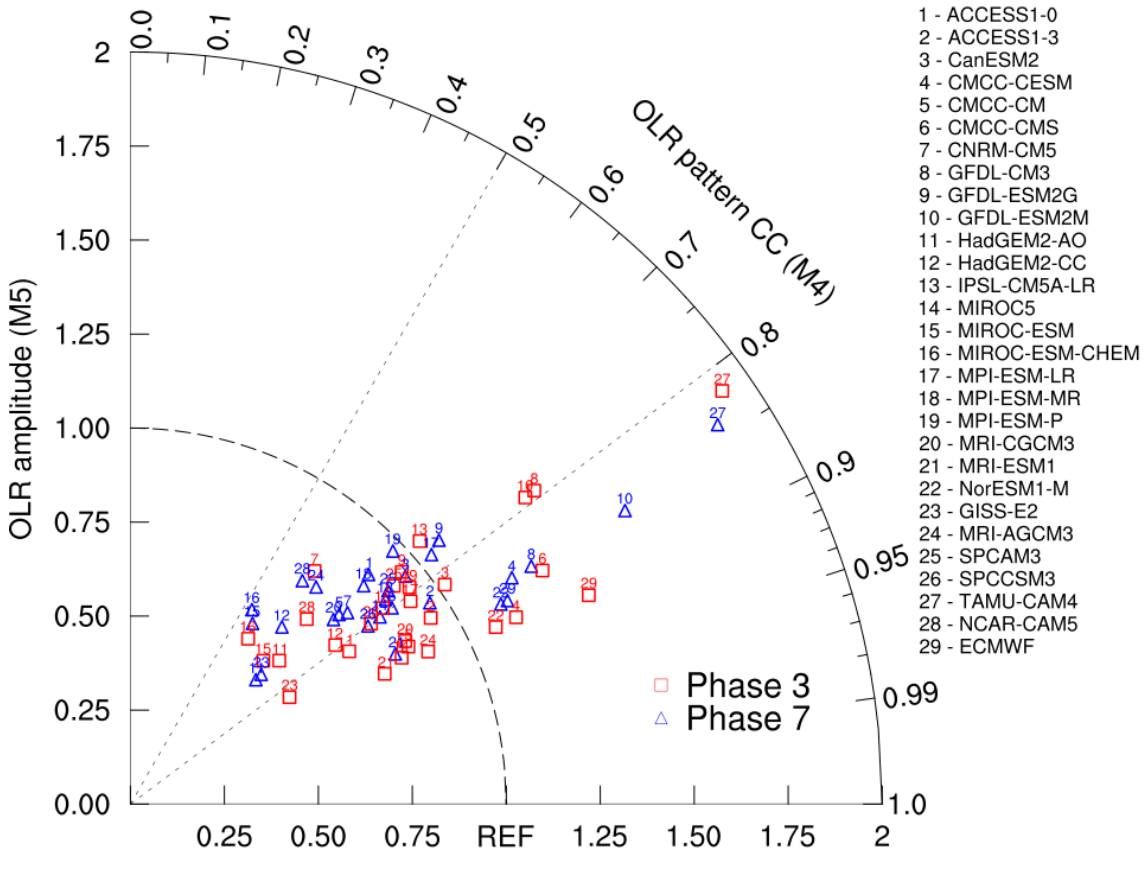

FIG. 4. Taylor diagram of OLR pattern CC (M4) and OLR amplitude (M5) for MJO phase 3 (red square) and 7 (blue triangle). The distance between each model and the reference point "REF" indicates the root-mean-square error (RMSE).

Accepted for publication in *Journal of Climate*. DOI 10.1175/JCLI-D-19-0865.1.

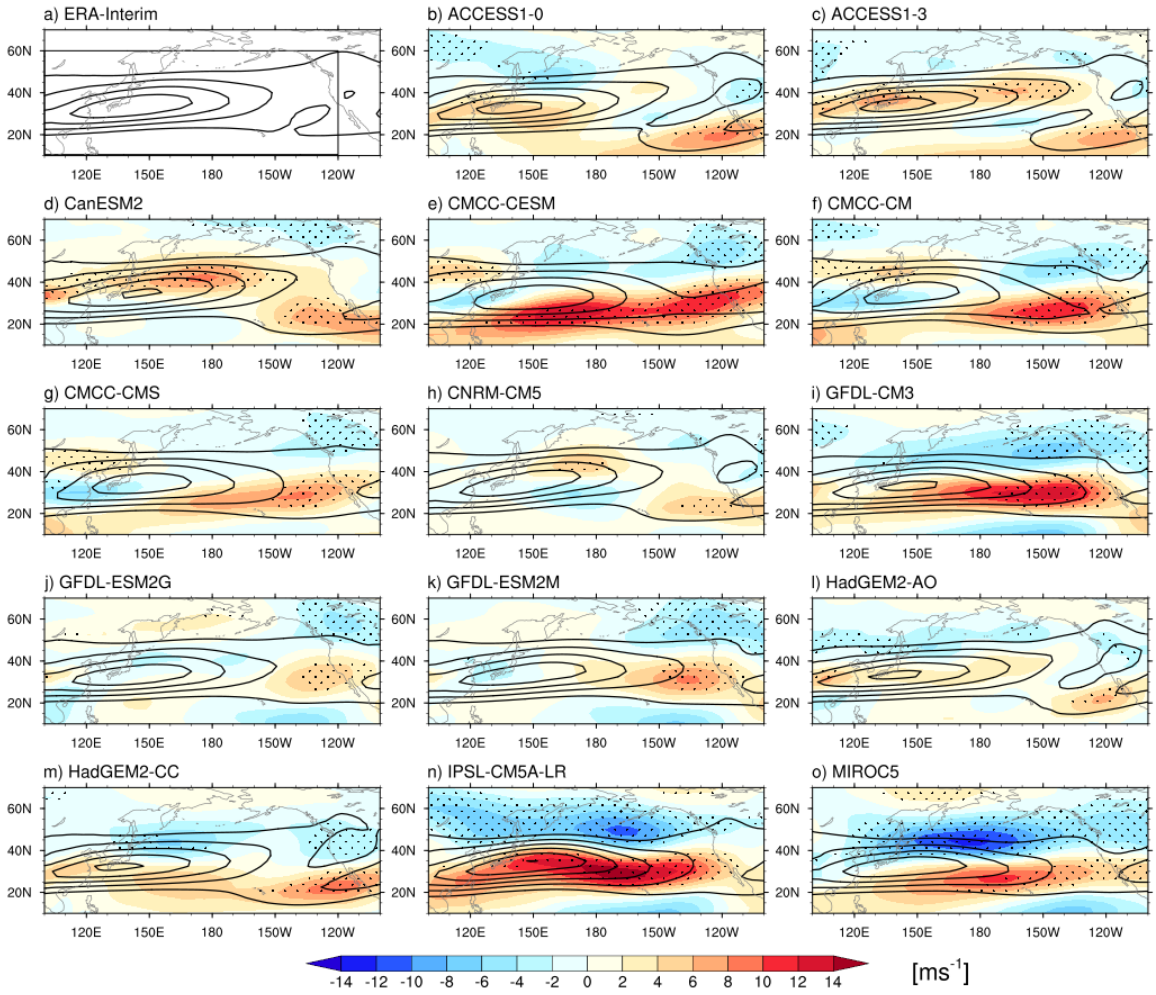

FIG. 5. Climatology of U250 (contour interval: 10 m s^{-1} starting from 20 m s^{-1}) in (a) observations and (b-dd) models. Shading denotes the model biases, defined as the difference between the modeled and observed U250. Dotted areas indicate significant biases exceeding the 95% confidence level according to the two-tailed Student's t-test. Black box in (a) represents the region over 100°E-120°W, 10°-60°N.

Accepted for publication in *Journal of Climate*. DOI 10.1175/JCLI-D-19-0865.1.

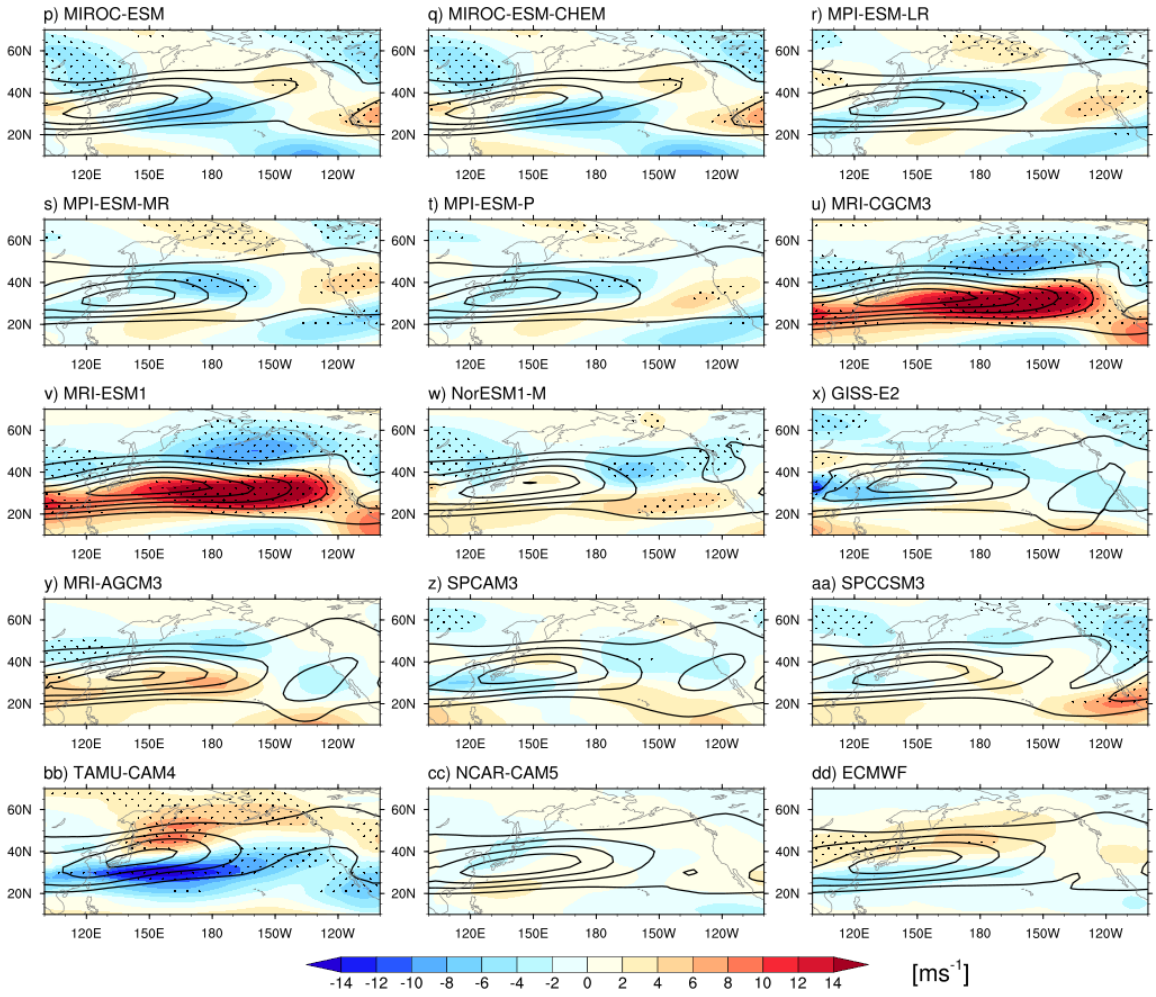

901

902 FIG. 5. (Continued).

Accepted for publication in *Journal of Climate*. DOI 10.1175/JCLI-D-19-0865.1.

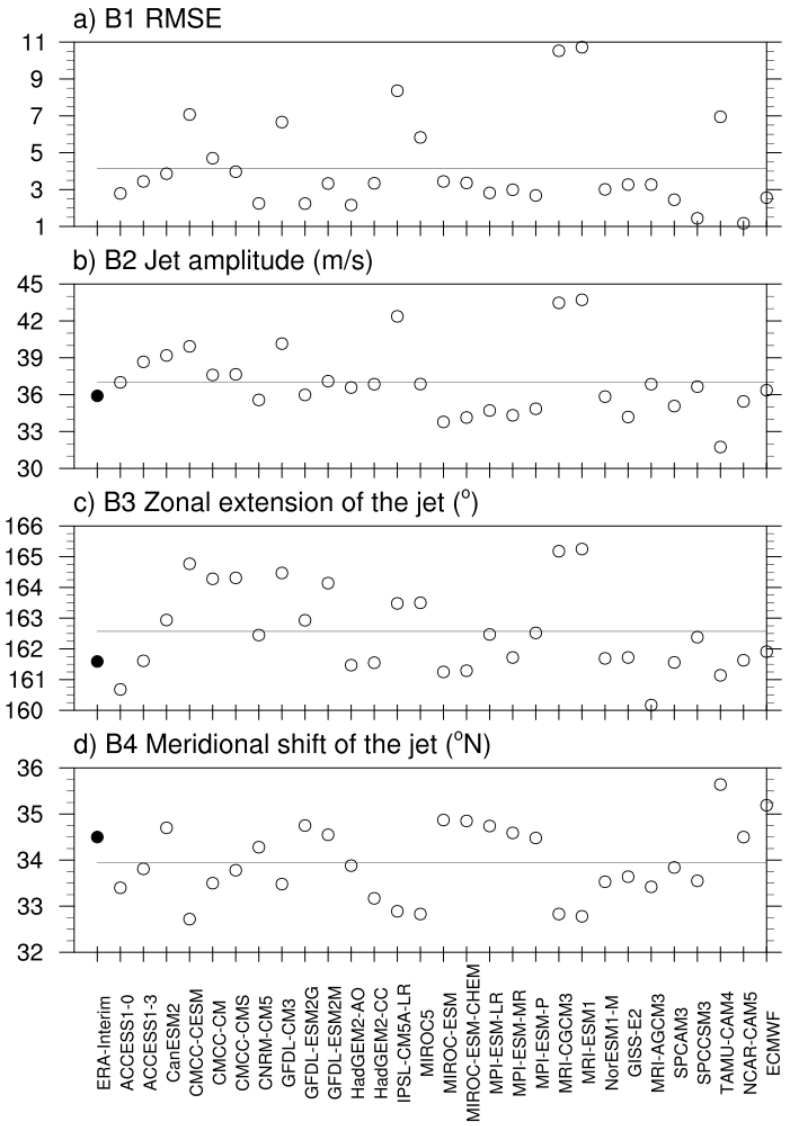

903

904 FIG. 6. (a) RMSE (B1), (b) jet amplitude (B2), (c) zonal extension of the jet (B3), and (d)
905 meridional shift of the jet (B4) for observations (closed circles) and each model
906 (open circles). Solid lines represent the multi-model mean.

907

Accepted for publication in *Journal of Climate*. DOI 10.1175/JCLI-D-19-0865.1.

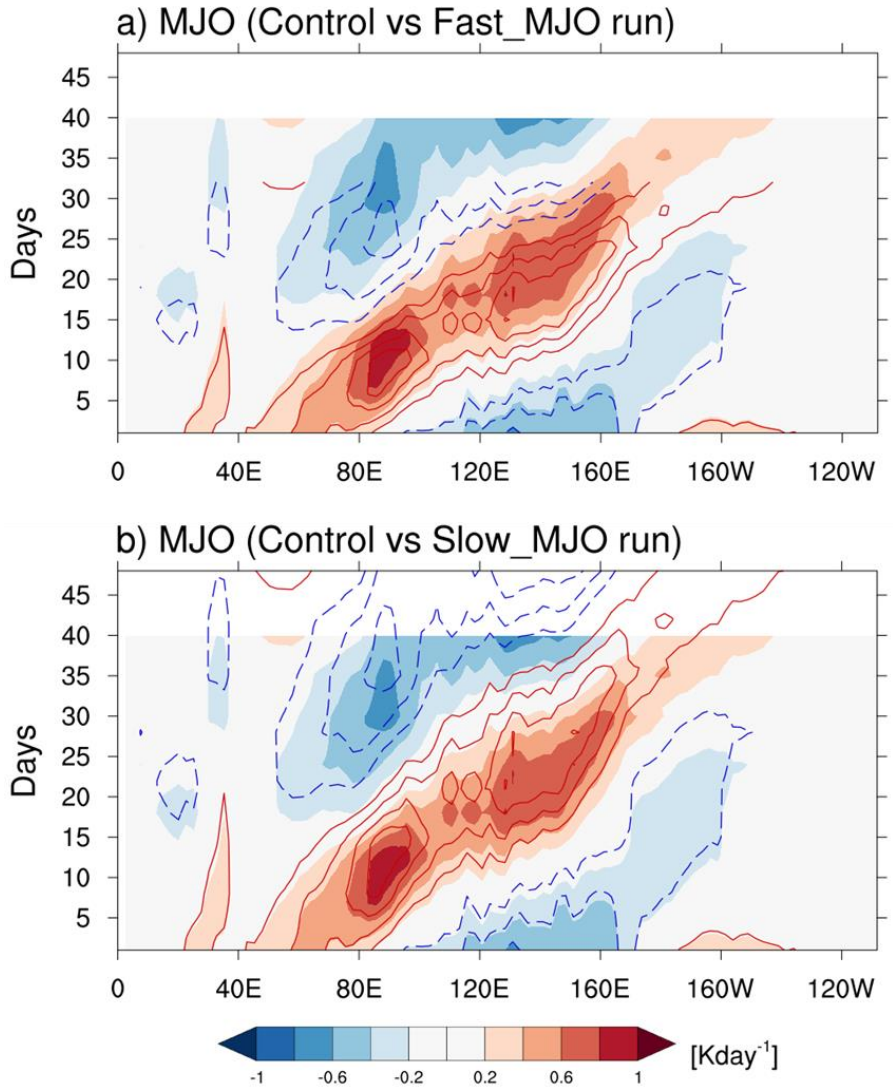

908
909 FIG. 7. The propagating MJO forcing used in LBM control run (shading, average over
910 10°S-10°N) and in the (a) *Fast_MJO* and (b) *Slow_MJO* runs (contour, interval:
911 0.2 K day^{-1}).

Accepted for publication in *Journal of Climate*. DOI 10.1175/JCLI-D-19-0865.1.

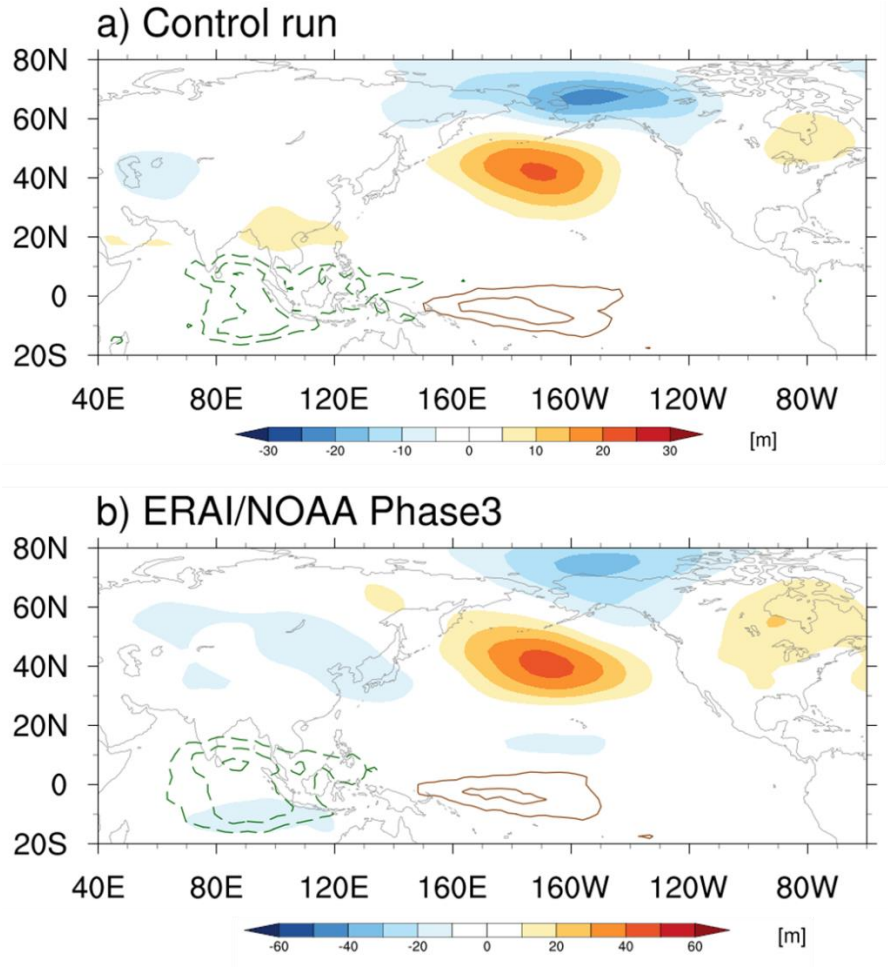

912

913 FIG. 8. (a) Phase 3 teleconnection in the LBM and the (b) observational reference (shading).

914 Contour in (a) is the 1000- to 200-hPa averaged anomalous observational Q_1 for

915 MJO phase 3 (average over model days 11-15): green (brown) represents MJO

916 heating (cooling) with interval of 0.4 K day^{-1}. Contour in (b) is the composite of

917 OLR anomaly over days in MJO phase 3: green (brown) represents enhanced

918 (suppressed) MJO convection with interval of 10 W m^{-2}.

Accepted for publication in *Journal of Climate*. DOI 10.1175/JCLI-D-19-0865.1.

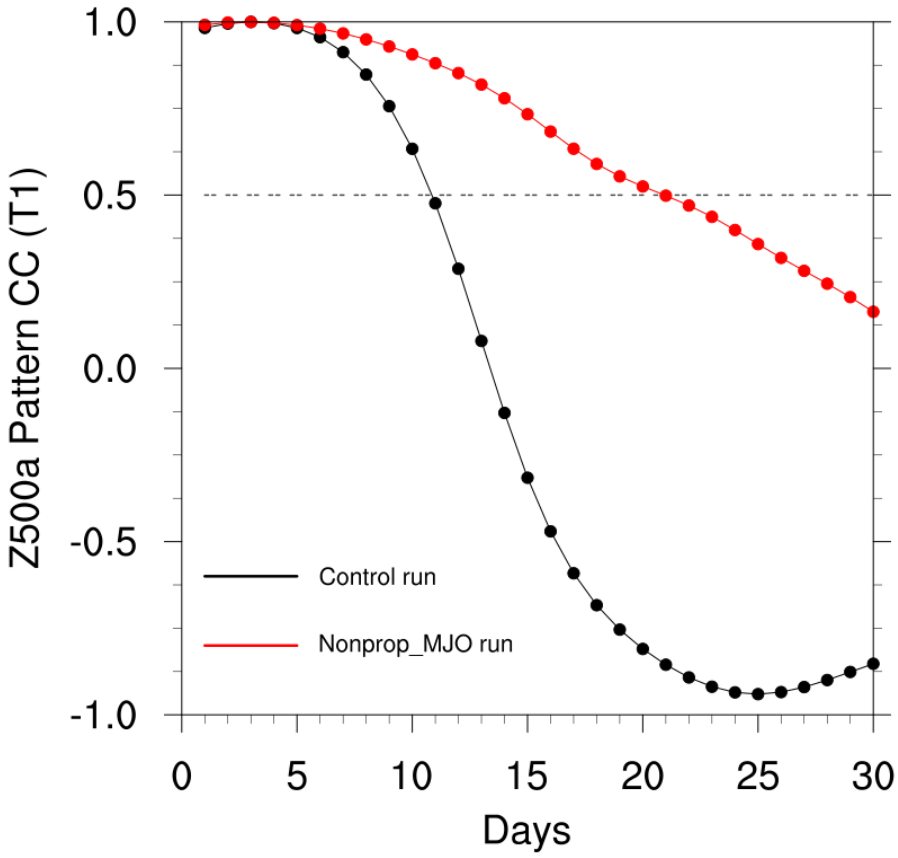

919

920 FIG. 9. Pattern CC between phase 3 teleconnection (i.e., Fig. 7a) and five-day running
921 average of Z500a over the PNA region in the control run (black line). Red line is
922 similar to black line but for the *Nonprop_MJO* run. Persistence is defined as
923 number of days that pattern CC being larger than 0.5 (dashed line).

Accepted for publication in *Journal of Climate*. DOI 10.1175/JCLI-D-19-0865.1.

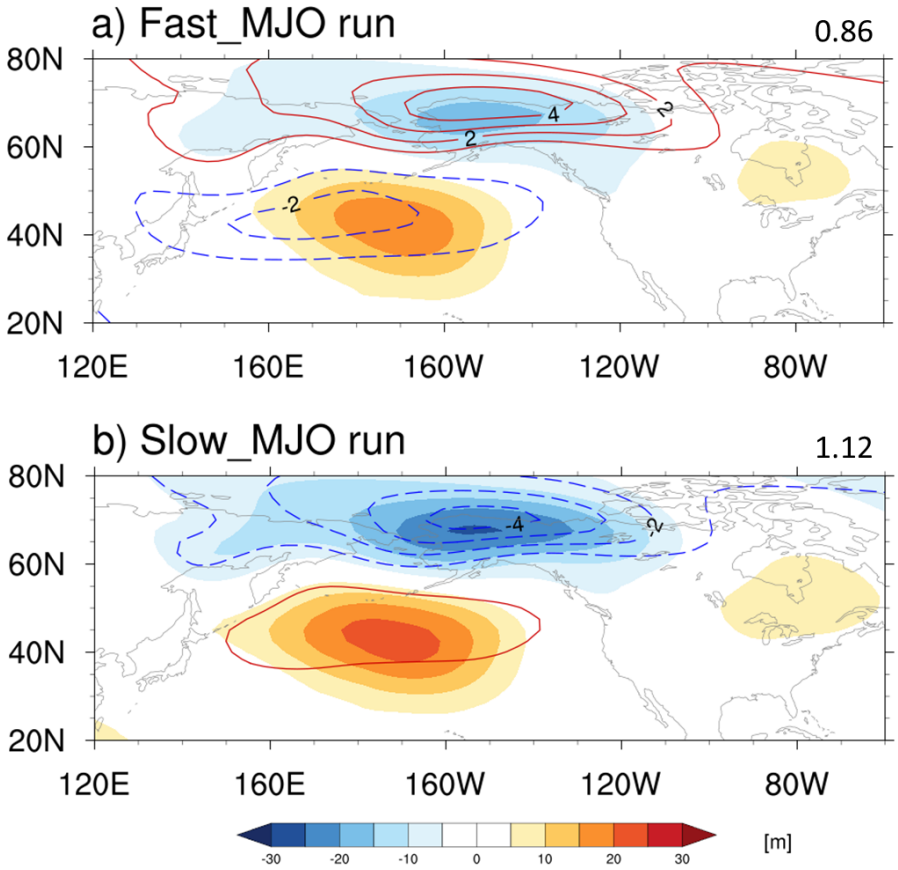

924

925 FIG. 10. Phase 3 teleconnection (shading) in the (a) *Fast_MJO* and (b) *Slow_MJO* runs.

926 Contours are the difference from the control run (interval: 1 m). Values on the top

927 right are MJO teleconnection metric T2 (Relative amplitude). T2 larger (smaller)

928 than 1 indicates stronger (weaker) response than the control run.

Accepted for publication in *Journal of Climate*. DOI 10.1175/JCLI-D-19-0865.1.

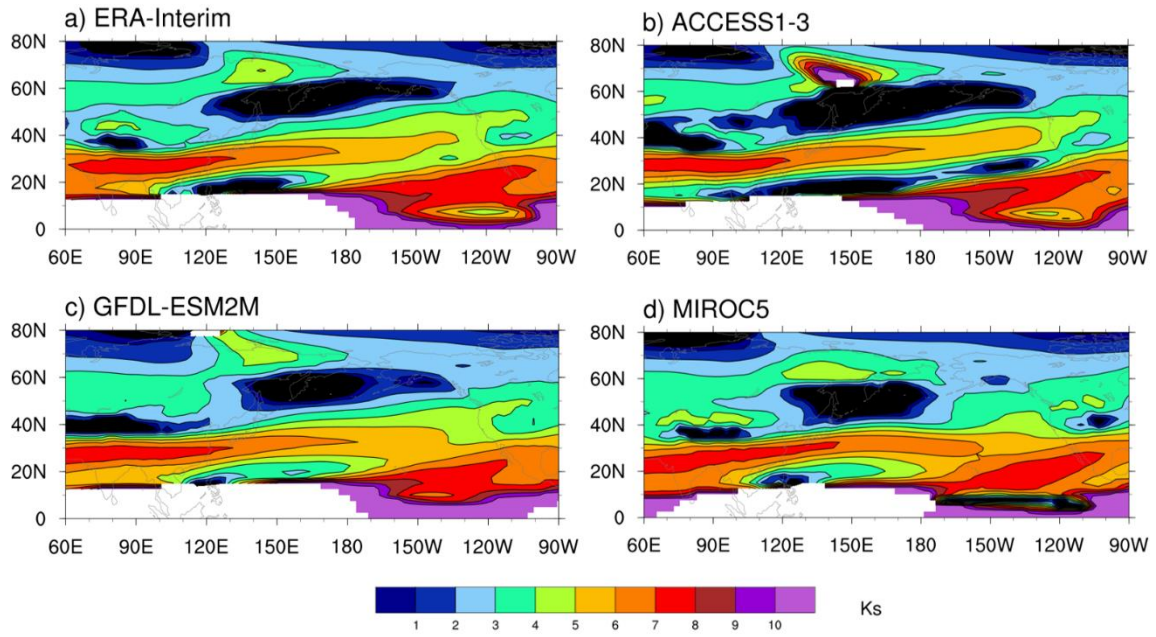

929

930 FIG. 11. Stationary wavenumber K_S derived from climatological U250 on Mercator
931 coordinates. Black areas are where meridional gradient of absolute vorticity β_M is
932 negative. Regions of easterly zonal winds are in white.

Accepted for publication in *Journal of Climate*. DOI 10.1175/JCLI-D-19-0865.1.

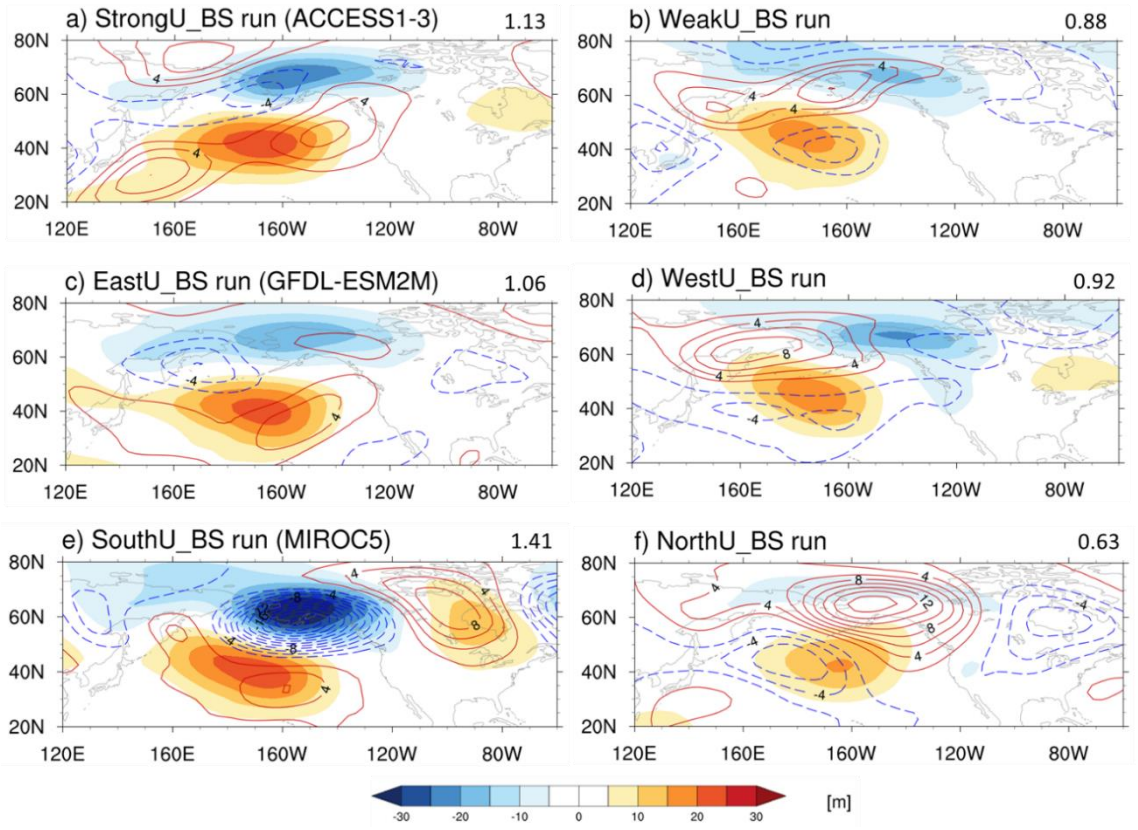

933

934 FIG. 12. Same as Fig. 9 except for the (a) *StrongU_BS*, (b) *WeakU_BS*, (c) *EastU_BS*, (d)

935 *WestU_BS*, (e) *SouthU_BS*, and (f) *NorthU_BS* runs (contour interval: 2 m).

936 Anomalous Q_1 used in these experiments are the same with the control run, i.e., the

937 observational eastward propagating Q_1.

Accepted for publication in *Journal of Climate*. DOI 10.1175/JCLI-D-19-0865.1.